JCTC Journal of Chemical Theory and Computation

pubs.acs.org/JCTC Article

Graph-Theoretic Molecular Fragmentation for Potential Surfaces Leads Naturally to a Tensor Network Form and Allows Accurate and Efficient Quantum Nuclear Dynamics

Anup Kumar, Nicole DeGregorio, Timothy Ricard, and Srinivasan S. Iyengar*

Cite This: J. Chem. Theory Comput. 2022, 18, 7243−7259 Read Online

ACCESS | Metrics & More | Article Recommendations | Supporting Information

ABSTRACT: Molecular fragmentation methods have revolutionized quantum chemistry. Here, we use a graph-theoretically generated molecular fragmentation method, to obtain accurate and efficient representations for multidimensional potential energy surfaces and the quantum time-evolution operator, which plays a critical role in quantum chemical dynamics. In doing so, we find that the graph-theoretic fragmentation approach naturally reduces the potential portion of the time-evolution operator into a tensor network that contains a stream of coupled lower-dimensional propagation steps to potentially achieve quantum dynamics with reduced complexity. Furthermore, the fragmentation approach used here has previously been shown to allow accurate and efficient computation of post-Hartree−Fock electronic potential energy surfaces, which in many cases has been shown to be at density functional theory cost. Thus, by combining the advantages of molecular fragmentation with the tensor network formalism, the approach yields an on-the-fly quantum dynamics scheme where both the electronic potential calculation and nuclear propagation portion are enormously simplified through a single stroke. The method is demonstrated by computing approximations to the propagator and to potential surfaces for a set of coupled nuclear dimensions within a protonated water wire problem exhibiting the Grotthuss mechanism of proton transport. In all cases, our approach has been shown to reduce the complexity of representing the quantum propagator, and by extension action of the propagator on an initial wavepacket, by several orders, with minimal loss in accuracy.

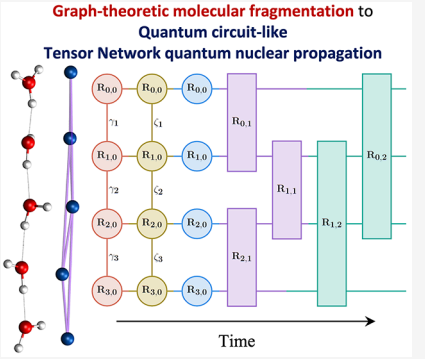

1. INTRODUCTION

The quantum mechanical treatment of electrons and nuclei is critical for a wide range of problems of interest in biological, materials, and atmospheric systems.[1] For example, hydrogen transfer processes and hydrogen bonded systems are ubiquitous,[2,3] but the detailed study of such processes is confounded by the presence of non-trivial quantum nuclear effects, such as hydrogen tunneling,[1,4−9] coupled with electron correlation.[10]

For the study of electron correlation in most molecular systems, chemical accuracy may be obtained using the well-known CCSD(T) method[11] with an associated computational cost that scales as $O(N^7)$, where N represents the number of electronic basis functions. The quantum dynamical treatment of nuclei, however, is thought to be exponentially complex.[12−15] As a result, the accurate study of quantum nuclear dynamics is complicated by the following challenges: (a) The computational cost associated with obtaining accurate electronic potential energy surfaces needed to define the dynamics is complicated by the fact that the number of configurations needed to depict the surfaces may grow exponentially with the number of quantum nuclear dimensions.[16−21] (b) The storage of the operators such as the quantum propagator and the wavepackets also may grow exponentially with dimensions,[22−25] and finally, (c) the action of the quantum propagator on a wavepacket, that is, the actual quantum dynamics step, also may require a set of operations that grow exponentially with the number of dimensions.[14,15,24,26] Associated with these challenges, multiple quantum computing platforms have been recently developed and may provide an approach toward the efficient treatment of the quantum nuclear dynamics[27−34] and electronic structure.[35−45]

Despite progress, critical challenges remain. For quantum nuclear dynamics, one complication that multidimensional problems[21,46−48] present is that the potential energy surface is entangled across dimensions. To address this issue, in this publication, we present a quantum propagation strategy that utilizes our recently developed graph-theoretic approach to molecular fragmentation as a means to provide the potential surface[46,49−57] and associated description of quantum propagation. This approach allows us to decouple the multidimensional quantum nuclear representation into a family of lower-dimensional quantum problems that may be streamed in

Received: May 9, 2022
Published: November 4, 2022

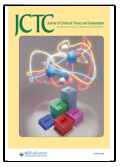

https://doi.org/10.1021/acs.jctc.2c00484
J. Chem. Theory Comput. 2022, 18, 7243−7259

parallel. There appear deep connections between our strategy and other techniques that reduce quantum circuit depth through circuit decoupling approximations.[58−62]

The paper is organized as follows: In Sections 2 and 3, we highlight our new approach which uses molecular fragmentation to create a quantum nuclear wavepacket propagation scheme to drastically reduce the complexity of quantum nuclear propagation. The approach is benchmarked for a protonated water wire problem in Section 4. Conclusions are given in Section 5.

Additional computational aspects are discussed in Appendix A and the Supporting Information.

2. MOLECULAR FRAGMENTATION NATURALLY YIELDS A TENSOR NETWORK REPRESENTATION FOR QUANTUM PROPAGATION

In refs 46, 49−57, 62, and 63, we have developed and demonstrated the utility of a graph theory-based molecular fragmentation[64−84] approximation that is based on many-body expansions[70,71,85−98] embedded within an our own n-layered integrated molecular orbital and molecular mechanics (ONIOM)[69,99−103] scheme. We have used the approach to compute conservative Born−Oppenheimer[49−51] and extended Lagrangian[50,51] ab initio molecular dynamics (AIMD) trajectories at the accuracy of CCSD and MP2 levels of theory but at the computational cost of density functional theory (DFT). We have also presented condensed-phase electronic structure studies at hybrid DFT accuracy at the computational cost of pure DFT functions.[56] We have demonstrated an adaptive, multi-topology-based molecular fragmentation approach for AIMD[57] and multidimensional potential energy surface calculations.[46,54]

The implementation of this methodology allows simultaneous use of Gaussian,[104] ORCA,[105] Psi4,[106] Quantum Espresso,[107] and OpenMX[108] within a single electronic structure, dynamics, and potential surface calculation. An efficient approach for quantum computation has also been derived from these methods,[62] and machine-learning generalizations have also been presented in ref 63. In this section, we utilize the graph-theory-based molecular fragmentation to provide an efficient representation for quantum nuclear dynamical propagation.

2.1. Quantum Time-Evolution Operator Represented Using Potential Surfaces from Graph-Theory-Based Molecular Fragmentation. A molecular system[56] is divided into a set of fragments. These fragments are treated as nodes within a graph. All nodes are then connected based upon a distance cut-off criterion, to form edges, and these edges help capture two-body interactions between the node fragments. The set of nodes, depicted as $\mathbf{V}_0$, and the set of edges, depicted as $\mathbf{V}_1$, are used to define a graph, $\mathcal{G}$. Higher-order local many-body interactions between the nodes are captured by considering contributions from a set of simplexes.[109−113] Simplexes are defined as geometric objects with an arbitrary number of vertices, where all pairs of vertices are connected. These include fragments formed from triangles within the set depicted as $\mathbf{V}_2$ which represents all faces within the graph, tetrahedral objects formed from four nodal fragments that reside within the set $\mathbf{V}_3$, and so on.

For a given molecular geometry, $\mathbf{R}$, influenced by ONIOM,[99,102,103] the system energy at some low level of electronic structure theory, *level*, 0, with energy $E^{level,0}$, is corrected using graph-theoretically generated[46,52−57] many-body expansions[70,85−88,90,94−98] to arrive at the energy expression[46,52−57]

$$E_{\mathcal{R},\mathcal{G}}(\mathbf{R}) = E^{level,0}(\mathbf{R}) + \sum_{r=0}^{\mathcal{R}} (-1)^r \sum_{\alpha \in \mathbf{V}_r} \Delta E^{1,0}_{\alpha,r}(\mathbf{R}_{\alpha,r}) \mathcal{M}^{\mathcal{R}}_{\alpha,r} \tag{1}$$

This expression has been shown to serve well as an approximation to the energy at a higher level of electronic structure theory, *level*, 1. In eq 1, $E_{\mathcal{R},\mathcal{G}}(\mathbf{R})$ is the energy associated with molecular geometry $\mathbf{R}$ using graphical decomposition $\mathcal{G}$. The quantity, $\mathcal{R}$, is the rank of the largest simplex included and captures the $(\mathcal{R}+1)$-body interaction terms between the nodal fragments. The quantity $E^{level,0}(\mathbf{R})$ is the energy of the full system at "*level*, 0" electronic structure theory. Furthermore, $\Delta E^{1,0}_{\alpha,r}(\mathbf{R}_{\alpha,r})$ is the difference between "*level*, 1" and "*level*, 0" electronic potential energies for the α-th $(r+1)$-body molecular fragment

$$\Delta E^{1,0}_{\alpha,r}(\mathbf{R}_{\alpha,r}) = E^{level,1}_{\alpha,r}(\mathbf{R}_{\alpha,r}) - E^{level,0}_{\alpha,r}(\mathbf{R}_{\alpha,r}) \tag{2}$$

The fragments are determined from the graphical decomposition, and the quantities $\mathbf{R}_{\alpha,r}$ represent the geometry of the α-th molecular fragment that is an $(r+1)$-body term in the many-body expansion. The quantity $\mathcal{M}^{\mathcal{R}}_{\alpha,r}$ in eq 1 is a multiplicity term to prevent over-counting in the graph-theoretic expression and includes the number of times the α-th $(r+1)$-body term appears in all fragments of the rank greater than or equal to r. The methodology for obtaining the graphs (and hence fragments that are denoted by the simplexes) is general and allows for treatment of non-uniform systems, based on the needed level of local many-body interactions. Although this graph-based fragmentation approach has been discussed in detail in refs 46, 49−57, 62, and 63, in Appendix A, we present an illustration of how this is done for complex systems. The overarching goal of our study here is to take steps toward performing quantum nuclear dynamics simulations where the potential surface is determined as per eq 1 and its multi-topology generalizations.[46,54,57]

In quantum dynamics, a nuclear wavepacket is evolved in time using the quantum propagator which may be written through Trotter factorization[114−118] as

$$\begin{aligned} e^{-\imath \hat{H} t/\hbar} &= e^{-\imath(\hat{K}+\hat{V})t/\hbar} \\ &= e^{-\imath \hat{V} t/2\hbar} e^{-\imath \hat{K} t/\hbar} e^{-\imath \hat{V} t/2\hbar} + O(t^3) \end{aligned} \tag{3}$$

Here, $\hat{K}$ and $\hat{V}$ are the kinetic and the potential energy operators, respectively. In the coordinate representation, the kinetic energy operator is separable across multiple dimensions, which makes $e^{-\imath \hat{K} t/\hbar}$ a direct product of propagators pertaining to individual dimensions.[20,119,120] The potential energy operator, on the other hand, is not in general separable across dimensions. This publication deals with efficient and accurate representations for $e^{-\imath \hat{V} t/2\hbar}$ and potential surfaces based on the graph-theoretic approach for molecular fragmentation presented in eq 1 and its multi-topology generalizations. We thus rewrite the diagonal elements of the potential energy portion of the time-evolution operator, that is, $e^{-\imath \hat{V} t/2\hbar}$, in the nuclear position representation which is now represented using a family of geometries, $\{\mathbf{R}\}$, represented on some multidimensional grid, using eq 1 to obtain

https://doi.org/10.1021/acs.jctc.2c00484
J. Chem. Theory Comput. 2022, 18, 7243−7259

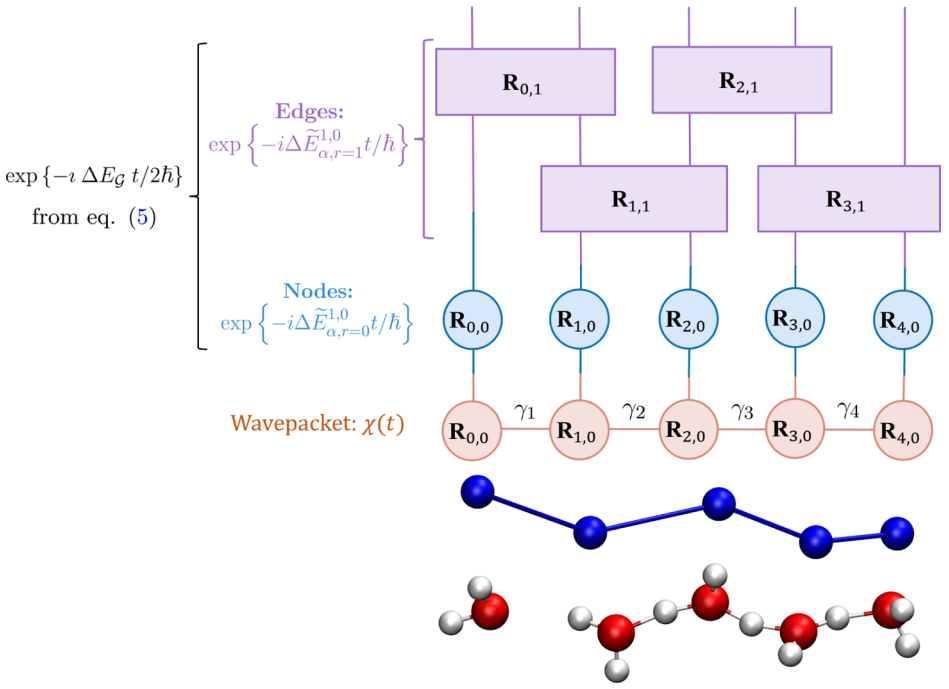

Figure 1. Figure provides an hierarchical arrangement of the operations, $\{\exp\{-\imath\{\Delta\tilde{E}^{1,0}_{\alpha,r}(\mathbf{R}_{\alpha,r})\}t/2\hbar\}\}$, in eq 5 where each such operation only acts on a portion of the quantum system depicted by the variables $\{\mathbf{R}_{\alpha,r}\}$. For example, for the water wire system (bottom of the picture is represented as a graph shown in dark blue nodes and edges right above the water wire), the propagators, $\exp\{-\imath\{\Delta\tilde{E}^{1,0}_{\alpha,r}(\mathbf{R}_{\alpha,r=0})\}t/2\hbar\}$, act only on quantum nuclear degrees of freedom represented within the nodes, $\mathbf{R}_{\alpha,r=0}$. Similarly, the family of propagators, $\exp\{-\imath\{\Delta\tilde{E}^{1,0}_{\alpha,r}(\mathbf{R}_{\alpha,r=1})\}t/2\hbar\}$, act only on quantum nuclear degrees of freedom represented within the edge ($r = 1$) depicted within the boxes shown as $\mathbf{R}_{\alpha,r=1}$. There are a total of four edges (shown as purple rectangles) in the above-shown figure. For example, the edge propagators containing the first (from the left) and the second edge dimension (depicted as $\mathbf{R}_{0,1}$), the second and the third edge dimension ($\mathbf{R}_{1,1}$), and so on.

$$
\begin{aligned}
\langle\mathbf{R}|\exp\{-\imath\hat{V}t/2\hbar\}|\mathbf{R}\rangle &\equiv \exp\{-\imath E_{\mathcal{R},\mathcal{G}}(\mathbf{R})t/2\hbar\} \\
&= \exp\left\{-\imath\left(E^{level,0}(\mathbf{R}) + \left\{\sum_{r=0}^{\mathcal{R}}(-1)^r\sum_{\alpha\in\mathbf{V}_r}\Delta E^{1,0}_{\alpha,r}(\mathbf{R}_{\alpha,r})\mathcal{M}^{\mathcal{R}}_{\alpha,r}\right\}\right)t/2\hbar\right\} \\
&= \exp\{-\imath(E^{level,0}(\mathbf{R}) + \Delta E_{\mathcal{G}}(\{\mathbf{R}_{\boldsymbol{\alpha,r}}\}))t/2\hbar\} \\
&= \exp\{-\imath E^{level,0}(\mathbf{R})t/2\hbar\}\,\exp\{-\imath\Delta E_{\mathcal{G}}(\{\mathbf{R}_{\alpha,r}\})t/2\hbar\}
\end{aligned}
\tag{4}
$$

where

$$
\begin{aligned}
&\exp\{-\imath\Delta E_{\mathcal{G}}(\{\mathbf{R}_{\alpha,r}\})\,t/2\hbar\} \\
&\quad= \prod_{r=0}^{\mathcal{R}}\prod_{\alpha\in\mathbf{V}_r}\exp\{-\imath\{\Delta\tilde{E}^{1,0}_{\alpha,r}(\mathbf{R}_{\alpha,r})\}\,t/2\hbar\} \\
&\quad= \prod_{\alpha\in\mathbf{V}_0}\exp\{-\imath\Delta\tilde{E}^{1,0}_{\alpha,r=0}(\mathbf{R}_{\alpha,0})\,t/2\hbar\} \\
&\qquad\prod_{\alpha\in\mathbf{V}_1}\exp\{-\imath\Delta\tilde{E}^{1,0}_{\alpha,r=1}(\mathbf{R}_{\alpha,1})\,t/2\hbar\} \\
&\qquad\cdots \\
&\qquad\prod_{\alpha\in\mathbf{V}_{\mathcal{R}}}\exp\{-\imath\Delta\tilde{E}^{1,0}_{\alpha,r=2}(\mathbf{R}_{\alpha,\mathcal{R}})\,t/2\hbar\}
\end{aligned}
\tag{5}
$$

and

$$
\Delta\tilde{E}^{1,0}_{\alpha,r}(\mathbf{R}_{\alpha,r}) = (-1)^r\Delta E^{1,0}_{\alpha,r}(\mathbf{R}_{\alpha,r})\mathcal{M}^{\mathcal{R}}_{\alpha,r} \tag{6}
$$

Note that the potential ($\hat{V}$) and the potential propagator ($\exp\{-\imath\hat{V}\,t/2\hbar\}$) are diagonal in position representation, and hence, the off-diagonal elements, $\langle\mathbf{R}'|\exp\{-\imath\hat{V}t/2\hbar\}|\mathbf{R}\rangle$, are identically 0. The quantity $\mathbf{R}_{\alpha,r}$ contains a far fewer number of nuclear degrees of freedom as compared to the full system depicted by the geometry $\mathbf{R}$. For example, if the many-body expansion is truncated at the two-body terms ($\mathcal{R} = 1$ in eq 4), then any given $\mathbf{R}_{\alpha,r}$ contains only those nuclear degrees of freedom within a fragment created from two-body interactions across nodal fragments.

This dimensional reduction is central to our approach here and has commonalities with other methods such as high-dimensional model representations,[121,122] basis-pruning approaches,[123−125] the POTFIT[20,126] approach commonly used in multi-configuration time-dependent Hartree,[126,127] and the molecular fragment surface approach from ref 128. The critical difference here is that our approach includes computing the

https://doi.org/10.1021/acs.jctc.2c00484
J. Chem. Theory Comput. 2022, 18, 7243−7259

potential based on a full ab initio potential, obtained from molecular fragmentation. That is, the dimensional reduction in the action of $e^{-\imath\hat{V}t/2\hbar}$ on a quantum nuclear wavepacket is entirely due to the factorization of the propagator as allowed by eq 1 and as is evident from eqs 4 and 5. In fact, Figure 1 is a tensor network that mimics the topology of the graph $\mathcal{G}$ from eq 1. Also see discussion in Appendix A. Note that there is no requirement on the tensor network[22,25] representation for the wavepacket and for the potential propagator to be of a specific form (such as a matrix product state[129]), and in fact, the tensor network topology is dictated by the chosen molecular graph representation (also see Appendix A).

2.2. Hierarchical, Quantum Circuit-like Decomposition from Eq 5. We now provide an analysis of the extent to which the above-mentioned formalism (massively) reduces the computational effort in quantum propagation when accurate potential energy values are computed on a multidimensional grid. Figure 1 complements our discussion (also see Appendix A). We begin by assuming $\mathcal{P}$ nuclear dimensions that are to be treated quantum mechanically in the entire molecular system. These dimensions are then assumed to be roughly equally divided into the $\mathcal{D}$-nodes leading to $\mathcal{P}/\mathcal{D}$ dimensions per node in a graph-theoretic fragmentation of the molecular structure. We further assume $\mathcal{N}$ discretizations per quantum nuclear dimension. This discretization is illustrated in Figure 2, where

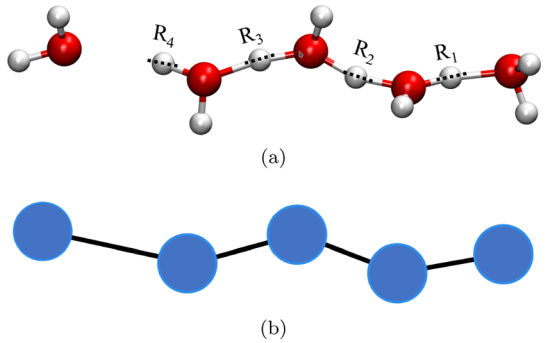

Figure 2. Grid-based representation of multidimensional quantum nuclear dynamics. All shared protons in the protonated water wire (a) are treated quantum mechanically along the grid dimensions shown. The multidimensional potential is treated here at the MP2 level, and approximations to the associated quantum nuclear dynamics and tensor network form on the potential presented. (b) shows the graphical description of (a), where only the nodes and edges are shown here. Compare (b) with the discussion in Appendix A where a graphical representation is presented for a more general system.

the individual protons participating in a hydrogen-bonded chain in a water wire are labeled $\{R_1, ..., R_4\}$ and are treated as a single multidimensional coupled quantum dynamical system. Each degree of freedom, for example, R_1, is discretized as shown with dots in Figure 2, and here, we assume $\mathcal{N}$ such discretizations per quantized nuclear dimension. This leads to a total of $\mathcal{N}^{\mathcal{P}}$ discretizations to define the entire potential energy surface, which is incidentally also the complexity of the general operation

$$\langle x|e^{-\imath\hat{V}t/2\hbar}|x\rangle\langle x||\chi\rangle \tag{7}$$

Here, x is a multidimensional grid point in the aforementioned $\mathcal{N}^{\mathcal{P}}$-dimensional space. That is, x represents one geometry within the $\mathcal{N}^{\mathcal{P}}$-dimensional space that determines the entire potential energy surface. Each node approximately contains information pertaining to $\mathcal{N}^{\mathcal{P}/\mathcal{D}}$ grid points. In the discussion mentioned below, $x \equiv \{x_1, x_2, ..., x_{\mathcal{D}}\}$ where x_i represents a grid discretization pertinent to the i-th node, the geometry for which is represented in eq 5 as $\mathbf{R}_{i,0}$. For example, a node comprising the right-most hydronium in Figure 2 only contains the grid points representing R_1. Hence, the nuclear geometry pertaining to such a node only includes the atoms that are within the fragment represented by the node.

Before we demonstrate the power of the aforementioned methodology, we begin with a Tensor-network[130] approximation to the initial wavepacket, $\langle x|\chi\rangle \equiv \chi(x)$, and more precisely, we start with a matrix product state approximation[129] to $\chi(x)$. The bottom row of nodes shown in the orange color inside Figure 1 represents a general initial quantum nuclear wavepacket, $\chi(x;t = 0)$, written as a matrix product state[129−131]

$$\chi(x) = \sum_{\overline{\gamma}} \chi^1_{\gamma_1}(x_1)\left(\prod_{j=2}^{\mathcal{D}-1} \chi^j_{\gamma_{j-1},\gamma_j}(x_j)\right)\chi^{\mathcal{D}}_{\gamma_{\mathcal{D}-1}}(x_{\mathcal{D}}) \tag{8}$$

where the so-called entanglement parameters[132−136] are $\overline{\gamma} \equiv \{\gamma_1, \gamma_2, \cdots \gamma_{\mathcal{D}-1}\}$. Similarly, the functions

$$[\chi^1_{\gamma_1}(x_1);\ \{\chi^j_{\gamma_{j-1},\gamma_j}(x_j)\}_{j=2\cdots\mathcal{D}-1};\ \chi^{\mathcal{D}}_{\gamma_{\mathcal{D}-1}}(x_{\mathcal{D}})] \tag{9}$$

are lower-dimensional functions that depend on variables, x_i, and span the nuclear dimensions embedded within each node separately. Diagrammatically, eq 8 is represented using the bottom row in Figure 1. Each orange-shaded circle in the bottom row represents a nodal dimension, as is clear from the notation, $\mathbf{R}_{\alpha,r=0}$, which is represented by the grid discretization, x_α, in eq 8. The line connecting two such circles in the bottom row is the respective γ_i component of entanglement vector $\overline{\gamma}$ in eq 8, and each vertical line is the grid dimension x_α pertaining to each node. Thus, eq 8 is a multi-configurational wavefunction, with correlation between the reduced dimensions dictated by the matrix product state description in eq 8. Computational aspects on how to obtain eq 8 using a sequence of bipartite singular value decomposition steps are discussed in ref 22 and summarized in Section S1.

We now illustrate the power of the propagation approach summarized using eqs 4 and 5 in stages. Our goal is to analyze the complexity of the operation, in eq 7, that is,

$$e^{-\imath V(x)t/2\hbar}\chi(x) = \exp\{-\imath E^{level,0}(x)t/2\hbar\} \times \exp\{-i\Delta E_{\mathcal{G}}(x)t/2\hbar\}\chi(x) \tag{10}$$

where we have used the fact that both $E^{level,0}$ and $\Delta E_{\mathcal{G}}$ are functions of the full dimensional grid represented here as x, as given by eq 1.

The action, $[\exp\{-i\Delta E_{\mathcal{G}}(x)t/2\hbar\}\chi(x)]$, is represented in Figure 1, and we explain the process in detail here using eq 5. The matrix product state form of the wavepacket is acted upon by the sequence of propagators such as $\exp\{-\imath\Delta\tilde{E}^{1,0}_{\alpha,r=0}t/2\hbar\}$ as shown in Figure 1. The action of the potential propagators for the node fragments, where $r = 0$, is represented by blue-colored circles in the second row from the bottom in Figure 1. Similarly, the action of the edge contributions, $\exp\{-\imath\Delta\tilde{E}^{1,0}_{\alpha,r=1}t/2\hbar\}$, is represented by the purple-filled rectangles in the top two rows in Figure 1. In all cases, the blue circles and purple rectangles in Figure 1 contain symbols such as "$\mathbf{R}_{0,1}$" which represents the simplex on which the specific propagator acts on. Thus, Figure 1 exemplifies the partitioned nature of our quantum propagation

https://doi.org/10.1021/acs.jctc.2c00484
J. Chem. Theory Comput. 2022, 18, 7243−7259

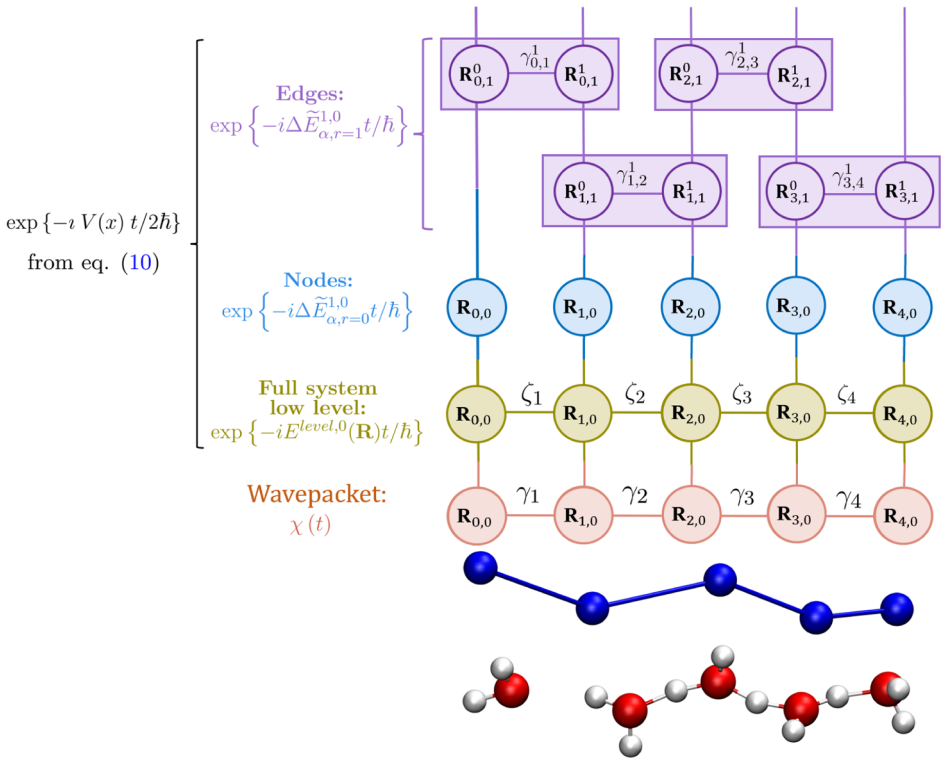

Figure 3. The figure presents an additional layer of sophistication beyond Figure 1 yielding the structure of the graph-theory-inspired tensor network form of the full quantum propagator. The term $\mathbf{R}^{i}_{\alpha,r}$ represents the i-th quantum nuclear dimension inside the α-th $(r+1)$-body fragment. The lowest row represents a molecular system that is represented as a graph (second row from the bottom) that leads to a matrix product state representation of the quantum nuclear wavepacket (third row from the bottom). All other rows inside the figure present the potential propagator terms for the full molecular system $\exp\{-\iota E^{level,0}(\mathbf{r})t/\hbar\}$, nodes ($\exp\{-\iota\Delta\tilde{E}^{1,0}_{\alpha,r=0}t/\hbar\}$), and edges ($\exp\{-\iota\Delta\tilde{E}^{1,0}_{\alpha,r=1}t/\hbar\}$) present inside eq 10. It should be noted that the difference between this figure and Figure 1 is that the potential propagators for the edges are further decomposed into tensor networks (matrix product states). For example, $\gamma^{1}_{0,1}, \gamma^{1}_{1,2}, \cdots$ are used to denote the coupling across the dimensions for edges ($r = 1$ in the superscript) indexed by $\alpha = 0, 1, \cdots$ (in the left subscript) and the indices for dimension, x_i, from eq 16 (right subscript which goes as 1, 2, $\cdots$). The second one from the bottom row shows the potential propagator for the full molecular system that contains five coupled quantum nuclear dimensions, and the coupling is shown through $\zeta_1, \zeta_2, \cdots\zeta_5$ symbols. See eq 14. Furthermore, the approach here also naturally lends itself to creation of a new quantum algorithm consistent with the work in ref 34.

scheme as achieved through the graph-theoretic depiction of the electronic structure.

Thus, given the matrix product state (MPS) approximation for $\chi(x)$ in eq 8, we may write

$$\prod_{\alpha\in\mathbf{V}_0}\exp\{-\iota\Delta\tilde{E}^{1,0}_{\alpha,r=0}t/2\hbar\}\times\chi(x)=\sum_{\overline{\gamma}}[\exp\{-\iota\Delta\tilde{E}^{1,0}_{\alpha=1,r=0}(x_1)t/2\hbar\}\chi^{1}_{\gamma_1}(x_1)]\times\left(\prod_{j=2}^{\mathcal{D}-1}[\exp\{-\iota\Delta\tilde{E}^{1,0}_{\alpha=j,r=0}(x_j)t/2\hbar\}\chi^{j}_{\gamma_{j-1},\gamma_j}(x_j)]\right)\times[\exp\{-\iota\Delta\tilde{E}^{1,0}_{\alpha=\mathcal{D},r=0}(x_{\mathcal{D}})t/2\hbar\}\chi^{\mathcal{D}}_{\gamma_{\mathcal{D}-1}}(x_{\mathcal{D}})] \tag{11}$$

where each square-bracketed term in eq 11, $[\cdots]$, is essentially a reduced-dimensional quantum propagation, where a set of reduced-dimensional quantum nuclear propagators are applied, in parallel, to the family of reduced-dimensional functions that are part of the matrix product state for the wavepacket, $\chi(x)$. The complexity reduction is already apparent from this expression if the number of possible values included for $\gamma_1, \gamma_2, \ldots, \gamma_{\mathcal{D}-1}$, that is, the entanglement dimensions, is *small*. This is generally the case in most chemical systems where entanglement entropy grows as the area of the Hilbert space as opposed to the volume,[137] and we will see this to be the case in the Results section as well. In this case, the complexity of the right side of eq 11 is approximately $O(\mathcal{N}^{\mathcal{P}/\mathcal{D}})$, given that $\mathcal{P}$ nuclear dimensions are divided across $\mathcal{D}$ nodes with $\mathcal{N}$ discretizations per nuclear degree of freedom, thus greatly reducing the exponential scaling complexity. Note that the $\mathcal{D}$ individual quantum propagation steps captured in eq 11, for example,

$$\phi^{j}_{\gamma_{j-1},\gamma_j}(x_j)=\exp\{-\iota\Delta\tilde{E}^{1,0}_{\alpha=j,r=0}(x_j)t/2\hbar\}\chi^{j}_{\gamma_{j-1},\gamma_j}(x_j) \tag{12}$$

may be computed in parallel, yielding a linear speedup of $\mathcal{D}$ over and above the $O(\mathcal{N}^{\mathcal{P}/\mathcal{D}})$ scaling. Also, note that eq 12 only contains functions of each nodal dimension and not those of the full system. Hence, the result from the action in eq 11 remains an

https://doi.org/10.1021/acs.jctc.2c00484
J. Chem. Theory Comput. 2022, 18, 7243−7259

MPS state, with entanglement dimensions, $\overline{\gamma}$, as also seen from the bottom two rows of Figure 1. Thus,

$$\prod_{\alpha\in\mathbf{V}_0} \exp\{-\iota\Delta\tilde{E}^{1,0}_{\alpha,r=0}\, t/2\hbar\} \times \chi(x) = \sum_{\overline{\gamma}} \phi^1_{\gamma_1}(x_1)\left(\prod_{j=2}^{\mathcal{D}-1} \phi^j_{\gamma_{j-1},\gamma_j}(x_j)\right)\phi^{\mathcal{D}}_{\gamma_{\mathcal{D}-1}}(x_{\mathcal{D}}) \tag{13}$$

The edge and face operations may be similarly described and act on reduced-dimensional functions as described in Figure 1. In this manner, the quantum propagators in Figure 1 can be extended to arbitrary-ranked $(\mathcal{R}+1)$-body fragments. Geometrically, one may envision the quantum propagation of a function defined on some $\mathcal{P}$-dimensional hypercube (domain) as a product of many different lower-dimensional-hypercube propagation steps, where each such hypercube is of dimensionality $[r \times \mathcal{P}/\mathcal{D}]$.

Although the computational complexity of the graph components such as nodes, edges, triangles, and so on is in general much smaller than it is for the full molecular system, an additional degree of reduction in complexity can be obtained by also constructing MPS[129] states of the edge and face propagators. This aspect is expressed in Figure 3 and is considered in more detail in the next section.

3. TENSOR NETWORK DECOMPOSITION OF THE OPERATORS, $\exp\{-\iota E^{level,0}(\mathbf{R})t/2\hbar\}$ and $\exp\{-\iota\Delta\tilde{E}^{1,0}_{\alpha,r}t/2\hbar\}$, FOR $r > 0$

In the above-mentioned section, we show how a significant portion of the potential energy time-evolution operator, $e^{-\iota\hat{V}t/2\hbar}$, can be simplified using the graph-theoretic molecular fragmentation procedure. This is done by exploiting the $\mathbf{R}_{\alpha,r}$ dependence of the various fragment energies, $\{\Delta\tilde{E}^{1,0}_{\alpha,r}(\mathbf{R}_{\alpha,r})\}$. However, as seen from eq 4, the $E^{level,0}(\mathbf{R})$-dependent propagator term, $\exp\{-\iota E^{level,0}(\mathbf{R})t/2\hbar\}$, does depend on the full nuclear space $\mathbf{R}$. Furthermore, the edge, face, and higher-order contributions to $\exp\{-\iota\Delta E_{\mathcal{G}}(\{\mathbf{R}_{\alpha,r}\})t/2\hbar\}$ also depend on multiple degrees of freedom within $\mathbf{R}_{\alpha,r}$. Thus, we utilize a tensor network[22,25] decomposition to write $\exp\{-\iota E^{level,0}t/2\hbar\}$ as

$$\exp\{-\iota E^{level,0}t/2\hbar\} = \sum_{\overline{\zeta}} \mathcal{V}^1_{\zeta_1}(x_1)\left(\prod_{j=2}^{\mathcal{D}-1} \mathcal{V}^j_{\zeta_{j-1},\zeta_j}(x_j)\right)\mathcal{V}^{\mathcal{D}}_{\zeta_{\mathcal{D}-1}}(x_{\mathcal{D}}) \tag{14}$$

where, as in eq 8, $\exp\{-\iota E^{level,0}t/2\hbar\}$, a multidimensional function in the coordinate representation, is written as a matrix product state using the one-dimensional functions $\mathcal{V}^1_{\zeta_1}(x_1)$, $\{\mathcal{V}^j_{\zeta_{j-1},\zeta_j}(x_j)\}$, and $\mathcal{V}^{\mathcal{D}}_{\zeta_{\mathcal{D}-1}}(x_{\mathcal{D}})$. Here, $\mathcal{V}^1_{\zeta_1}(x_1)$ (or $\mathcal{V}^{\mathcal{D}}_{\zeta_{\mathcal{D}-1}}(x_{\mathcal{D}})$) represents the ζ_1-th (or $\zeta_{\mathcal{D}}$-th) one-dimensional function along the first (or last) dimension, and $\{\mathcal{V}^j_{\zeta_{j-1},\zeta_j}(x_j)\}$ represents a one-dimensional function along the j-th dimension that entangles the $(j-1)$-th and j-th dimensions. Thus,

$$\exp\{-\iota E^{level,0}t/2\hbar\} \times \eta(x) = \sum_{\overline{\zeta},\overline{\gamma}} \mathcal{V}^1_{\zeta_1}(x_1)\chi^1_{\gamma_1}(x_1)\left(\prod_{j=2}^{\mathcal{D}-1} \mathcal{V}^j_{\zeta_{j-1},\zeta_j}(x_j)\chi^j_{\gamma_{j-1},\gamma_j}(x_j)\right)(\mathcal{V}^{\mathcal{D}}_{\zeta_{\mathcal{D}-1}}(x_{\mathcal{D}})\chi^{\mathcal{D}}_{\gamma_{\mathcal{D}-1}}(x_{\mathcal{D}}) \tag{15}$$

In the end, we have an entangled state as that in eq 8 on the left side of eq 15 that may be fed in as input into $\exp\{-i\Delta E_{\mathcal{G}}(x)t/2\hbar\}$ as discussed in the previous section. The MPS form written in eq 15 is illustrated inside Figure 3 in the bottom two rows of the tensor diagram shown in olive and orange colors.

However, at this stage, a similar MPS approximation can also be constructed for the edge and face propagation ($\exp\{-\iota\Delta\tilde{E}^{1,0}_{\alpha,r}t/2\hbar\}$ for $r > 0$) operations so as to further reduce their respective computational complexities. Thus, for $r > 0$, the potential propagators can also be written as the matrix product state similar to eq 14 as

$$\exp\{-\iota\Delta\tilde{E}^{1,0}_{\alpha,r}\, t/2\hbar\} = \sum_{\overline{\gamma}^r_\alpha} \tilde{\mathcal{V}}^1_{\gamma^r_{\alpha,1}}(x_1)\left(\prod_{j=2}^{\mathcal{D}-1} \tilde{\mathcal{V}}_{\gamma^r_{\alpha,j-1},\gamma^r_j}(x_j)\right)\tilde{\mathcal{V}}^{\mathcal{D}}_{\gamma^r_{\alpha,\mathcal{D}-1}}(x_{\mathcal{D}}) \tag{16}$$

The entire process of quantum propagation, using eq 5, along with the tensor-network decomposition of propagators and wavepackets, is depicted in Figure 3. The bottom two rows in Figure 3 depict the water wire and its molecular graph representation. The third row from the bottom contains the MPS form (shown in orange) of the wavepacket which is first acted on by the tensor network form of the full system low level (presented in the olive color) as shown in eq 15. As noted above, at the end of this step, the state remains a tensor network but with expanded entanglement dimensions $(\overline{\gamma}, \overline{\zeta})$. Following this, the action of the node fragment potential propagators (shown in blue) is depicted in the fifth row from the bottom. Right above the node propagators are MPS-approximated forms of the edge-potential propagators shown inside purple rectangles. Each rectangle depicts that the tensor inside it belongs to a specific fragment. For example, the bottom left purple rectangular box contains the potential propagator whose bond dimensions are $\gamma^1_{\alpha,1}$. Also see eq 16. Here, the subscripts represent the index for the fragment entity, α, followed by the bond dimension, and the superscript represents the rank of the simplex forming that fragment (such as $r = 1$ for edges). The nodes inside the rectangle, for example, $\mathbf{R}^0_{\alpha,r}$, denote the zeroth-nodal dimensional MPS function for the α-th simplex of rank r.

Following this discussion, we may write the final expression as an MPS state according to

$$\begin{aligned} &e^{-\iota V(x)t/2\hbar}\chi(x) \\ &= \exp\{-\iota\Delta E_{\mathcal{G}}(x)t/2\hbar\}\exp\{-\iota E^{level,0}(x)t/2\hbar\}\chi(x) \\ &= \prod_{r=0}^{\mathcal{R}}\prod_{\alpha\in\mathbf{V}_r} \exp\{-\iota\{\Delta\tilde{E}^{1,0}_{\alpha,r}(\mathbf{R}_{\alpha,r})\}t/2\hbar\} \\ &\quad \exp\{-\iota E^{level,0}(x)t/2\hbar\}\chi(x) \end{aligned} \tag{17}$$

https://doi.org/10.1021/acs.jctc.2c00484
J. Chem. Theory Comput. 2022, 18, 7243−7259

which then leads to the final expression

$$
\begin{aligned}
&e^{-\iota V(x)t/2\hbar}\chi(x) = \\
&\sum_{\overline{\zeta},\overline{\gamma},\{\overline{\gamma_\alpha^r}\}} \left\{ \left(\prod_{r=0}^{\mathcal{R}} \prod_{\alpha\in\mathbf{V}_r} \tilde{\mathcal{V}}^{1}_{\gamma^r_{\alpha,1}}(x_1) \right) \mathcal{V}^{1}_{\zeta_1}(x_1)\chi^{1}_{\gamma_1}(x_1) \right\} \\
&\left[\prod_{j=2}^{\mathcal{D}-1} \left\{ \left(\prod_{r=0}^{\mathcal{R}} \prod_{\alpha\in\mathbf{V}_r} \tilde{\mathcal{V}}_{\gamma^r_{\alpha,j-1},\gamma^r_j}(x_j) \right) \mathcal{V}^{j}_{\zeta_{j-1},\zeta_j}(x_j)\chi^{j}_{\gamma_{j-1},\gamma_j}(x_j) \right\} \right] \\
&\left\{ \left(\prod_{r=0}^{\mathcal{R}} \prod_{\alpha\in\mathbf{V}_r} \tilde{\mathcal{V}}^{\mathcal{D}}_{\gamma^r_{\alpha,\mathcal{D}-1}}(x_{\mathcal{D}}) \right) \mathcal{V}^{\mathcal{D}}_{\zeta_{\mathcal{D}-1}}(x_{\mathcal{D}})\chi^{\mathcal{D}}_{\gamma_{\mathcal{D}-1}}(x_{\mathcal{D}}) \right\}
\end{aligned}
\tag{18}
$$

or

$$
\begin{aligned}
e^{-\iota V(x)t/2\hbar}\chi(x) = &\sum_{\overline{\zeta},\overline{\gamma},\{\overline{\gamma_\alpha^r}\}} \chi^{1}_{\gamma^r_{\alpha,1},\zeta_1,\gamma_1}(x_1) \\
&\left(\prod_{j=2}^{\mathcal{D}-1} \chi^{j}_{\gamma^r_{\alpha,j-1},\gamma^r_j,\zeta_{j-1},\zeta_j,\gamma_{j-1},\gamma_j}(x_j) \right) \\
&\chi^{\mathcal{D}}_{\gamma^r_{\alpha,\mathcal{D}-1},\zeta_{\mathcal{D}-1},\gamma_{\mathcal{D}-1}}(x_{\mathcal{D}})
\end{aligned}
\tag{19}
$$

which is an MPS with each individual dimensional propagation defined inside curly brackets on the second equation, $\{\cdots\}$, and entanglement variables, $\overline{\zeta}$, $\overline{\gamma}$, $\{\overline{\gamma_\alpha^r}\}$, reassigned explicitly on the right side. For example,

$$
\begin{aligned}
&\chi^{1}_{\gamma^r_{\alpha,1},\zeta_1,\gamma_1}(x_1) \equiv \\
&\left(\prod_{r=0}^{\mathcal{R}} \prod_{\alpha\in\mathbf{V}_r} \tilde{\mathcal{V}}^{1}_{\gamma^r_{\alpha,1}}(x_1) \right) \mathcal{V}^{1}_{\zeta_1}(x_1)\chi^{1}_{\gamma_1}(x_1)
\end{aligned}
\tag{20}
$$

and so on. This is perhaps the most critical step in quantum propagation eq 3, and as discussed, immediately following eq 7, the tensor network formalism that naturally arises from the graph decomposition scheme reduces complexity enormously. Specifically, the $\mathcal{N}^{\mathcal{P}}$ dimensional complexity of eq 3 may, in principle, be reduced to $\mathcal{N}^{\mathcal{R}/\mathcal{D}}$, when rank-$\mathcal{R}$ operations are needed in eqs 2, 4, and 5. See eq 19. However, it is also clear from eq 19 that the entanglement dimensions grow

$$
\overline{\gamma} \rightarrow \overline{\zeta}, \overline{\gamma}, \{\overline{\gamma_\alpha^r}\} \tag{21}
$$

and numerical schemes to curtail this growth will be discussed in a future publication (this aspect is also noted in ref 138).

Here, we mention the tensor network-based quantum dynamics approaches in refs 24 and 138. In ref 24, a model potential is used that contains one- and two-body interactions that involve a quartic potential for each proton and nearest-neighbor proton−proton interactions. When this potential is exponentiated (or used within the Chebyshev scheme in ref 24), it only involves the action of one and two quantum degrees of freedom at any given moment. Thus, in ref 24, the computational complexity is reduced by suitable choice of the model potential. In ref 138, quantum dynamics is performed using matrix product states and matrix product operators, and the potential surfaces are obtained using Taylor expansion[139,140] around a reference (optimized) geometry. As mentioned in ref 138, for long-time dynamics, the wave function explores regions of the potential energy surfaces that cannot be efficiently obtained using the power series approximation. On the contrary, our approach is a "direct" approach[17,141,142] where appropriate grid spread is chosen to make sure that the wave function is contained while incorporating the appropriate anharmonicity of the multidimensional potential. Even in comparison with the direct grid-based approaches in refs 141 and 142 where potential surfaces are obtained using machine learning-based potentials using CASSCF at the 3-21g basis set, the potential energy surfaces used for this publication are at post-Hartree−Fock accuracy [MP2/6-31++g(d,p)] but at a DFT cost. Also, note that the tensor-network representation for the wavepacket in eq 8 (in turn, the propagator in eq 5 and Figures 1 and 3) follows the molecular graph $\mathcal{G}$ and is general and is not restricted to have a matrix product state form. This aspect is also discussed in Appendix A for other systems.

Additionally, in the Results section mentioned below, as a step toward numerically benchmarking and analyzing the accuracy of the theory presented here, we also inspect the MPS form of the potential given by

$$
\begin{aligned}
&E_{\mathcal{R},\mathcal{G}}(\mathbf{R}) = \\
&\sum_{\overline{\zeta}} \xi^{1}_{\zeta_1}(x_1) \left(\prod_{j=2}^{\mathcal{D}-1} \xi^{j}_{\zeta_{j-1},\zeta_j}(x_j) \right) \xi^{\mathcal{D}}_{\zeta_{\mathcal{D}-1}}(x_{\mathcal{D}})
\end{aligned}
\tag{22}
$$

and similarly the potential propagator

$$
\begin{aligned}
&\exp\{-\iota E_{\mathcal{R},\mathcal{G}}(\mathbf{R})t/2\hbar\} = \\
&\sum_{\overline{\zeta}} \vartheta^{1}_{\zeta_1}(x_1) \left(\prod_{j=2}^{\mathcal{D}-1} \vartheta^{j}_{\zeta_{j-1},\zeta_j}(x_j) \right) \vartheta^{\mathcal{D}}_{\zeta_{\mathcal{D}-1}}(x_{\mathcal{D}})
\end{aligned}
\tag{23}
$$

4. MULTIDIMENSIONAL POTENTIAL ENERGY SURFACES FOR A PROTONATED WATER WIRE FROM TENSOR NETWORK DECOMPOSITION OF GRAPH-THEORETIC FRAGMENTATION

The molecular system studied in this paper is a protonated water wire[143−150] with an associated molecular graph shown in Figure 2. In Appendix A, we show how this formalism can also be used

https://doi.org/10.1021/acs.jctc.2c00484
J. Chem. Theory Comput. 2022, 18, 7243−7259

in more complex systems. Protonated water wires are an important class of molecular systems as these are found in many constrained environments such as biological membranes and enzyme active sites,[143−145] ion channels,[146] carbon nanotubes,[147−149] and fuel cells.[150] Water wires are also present in the photosynthetic reaction center of *Rhodobacter sphaeroides* where they are responsible for proton transfer to a secondary quinone group.[144] Furthermore, the lightweight hydrogen nucleus makes quantum nuclear effects important in such cases;[151−154] additionally, the multidimensional quantum nuclear effects in such systems are also known to be critical.[155,156]

In our studies for the potential energy surface calculations from eq 1, we have used DFT with the hybrid exchange−correlation functional (B3LYP) as "*level*,0" and Møller−Plesset perturbation theory (MP2) as "*level*,1" of the electronic structure. Both levels of theory utilize the Pople style 6-31++g(d,p) basis set as part of eq 1. This is not a requirement, and in refs 51, 56, 62, and 63, other levels of theory and basis have been explored. As discussed in refs 46 and 54, we use the description of potential energy surfaces using multiple graphs.

In the Supporting Information, we present critical computational aspects of our approach and contrast these with other existing techniques. One critical piece of the computational efficiency arises from the number of direct product functions needed in a matrix product state such as in eq 14. We present a scheme to appropriately tailor the number of such direct product functions, reorder these as per the discussion (see eq S11), and introduce a singular value ratio, eq S11, that gauges the extent to which each product state contributes to the overall accuracy. The remaining portion of the Results section is organized as follows: we use this measure in Sections 4.1 and 4.2 to compute the accuracy and efficiency of the scheme presented here using the error estimates presented in Section S4.

4.1. Multidimensional Potential Energy Surfaces. The water wire system is treated as one coupled quantum mechanical problem for the four hydrogen-bonded nuclear degrees of freedom shown in Figure 2. These nuclear degrees of freedom are treated in a sequential fashion allowing for the concerted, correlated treatment as indicated by the Grotthuss mechanism[157] of proton transfer in water clusters. The grid parameters for the potential energy surfaces used to define the coupled nuclear degrees of freedom are provided in Table 1 and shown in Figure 2a. Thus, physical dimensions R_1, R_2, ..., and R_4 are along the proton transfer coordinates for the shared protons inside the water wire system, shown in Figure 2a. We increase the complexity of the coupled proton quantum nuclear problem, one dimension at a time, and the exponential increment in grid size with the dimensions is apparent from Table 1.

Table 1. Grid Parameters for Potential Energy Surface Calculations Performed in Ref 46[a]

dimensionality	grid dimensions	grid size
2{R_1, R_2}	0.8 Å × 0.8 Å	99^2 = 9801
3{R_1, R_2, R_3}	0.8 Å × 0.8 Å × 0.8 Å	49^3 = 117,649
4{R_1, R_2, R_3, R_4}	0.8 Å × 0.8 Å × 0.8 Å × 0.8 Å	49^4 = 5,764,801

[a]The physical dimensions along the proton transfer coordinates of a water wire molecule $[(H_2O)_5H^+]$ are shown using dashed lines in Figure 2a.

In this section, the proton potential energy surfaces, $E_{\mathcal{R},\{\mathcal{G}_\beta\}}(\mathbf{R})$, are treated using the MPS formalism.

For the two-dimensional grid referred to as {R_1, R_2} in Table 1, the potential energy surface is shown in Figure 4a along with the first singular vector along R_1 in Figure 4b. Upon comparing Figure 4a,b, it is clear that the first singular vector captures the primary characteristics of the underlying potential energy surface along R_1. The higher values of the potential energy, located along the edges of the grid, are captured by other singular vectors along with lower-energy regions of the surface.

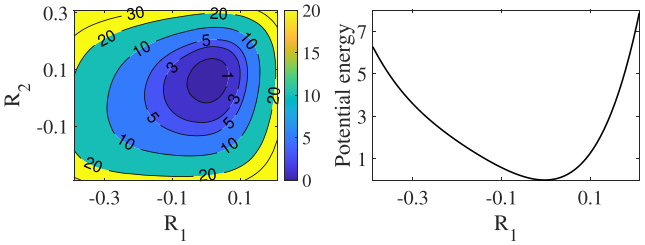

(a)Potential energy surface (kcal/mol) for R_1 and R_2 in fig. 2.

(b)First Singular vector along R_1. Vertical axis is in kcal/mol.

Figure 4. The figure on the left shows the actual potential energy surface for the R_1 and R_2 quantum nuclear degrees of freedom. The right figure shows the first singular vector along R_1. Notice here that the singular vector along the R_1 dimension is similar to an average slice along the minimum in panel (a). This is an example of the tensor network decomposition capturing the most critical features of the input data function.

In fact, the singular vector shown in Figure 4b has similar characteristics as the so-called "single particle potentials" described in the POTFIT[20,126] methodology but differs in that the reduced-dimensional vectors here are computed directly from the highly coupled potential as described in eq S6 inside Section S2. In this way, the needed entanglement is retained based on the measures discussed in Section S3, specifically eq S20.

Errors computed using the measures introduced in Section S4, namely, eqs S22 and S24, are shown in Table 2. Here, only three direct product states ($\mathcal{A} = 3$) are needed for the errors in the sub-kJ/mol accuracy range for the entire potential surface. Thus, based on these results and the Ξ values in Table 2, the dimensions R_1 and R_2 appear to be relatively uncorrelated to each other. Further supporting this, the ground eigenstate weighted error, Γ_{GS} (eq S24), requires one single direct product state to allow for sub-kcal/mol accuracy with respect to the MP2 potential, and $\mathcal{A} = 3$ yields far higher accuracy. This effectively shows how the method here can be used to probe correlations between nuclear degrees of freedom.

The errors in eigenvalues and the eigenvectors are represented as $\Delta\lambda_i$ and $\Delta\Lambda_i$ and are defined using eqs S25 and S26, respectively, in Section S4. In the case of the two-dimensional {R_1, R_2} system, the eigenvalue and the eigenvector errors for the ground state and the first excited state are provided in the last four columns of Table 2. Here, the MPS potential energy surfaces used to generate the eigenstates have errors shown in columns three and four in Table 2. The MPS potential energy surfaces produce eigenstates that are almost exact with 6.1% ($\mathcal{A} = 3$) of the total grid size (listed in Table 1). More importantly, the ground-state eigenvector is exact for an MPS with only one low-rank tensor along each dimension. For all measures of error, the two-dimensional potential energy surface

https://doi.org/10.1021/acs.jctc.2c00484
J. Chem. Theory Comput. 2022, 18, 7243−7259

Table 2. Results for a Potential Energy Surface for (R_1, R_2) Represented as a Tensor Network[a]

$\mathcal{A}$[b]	Ξ_l[c] eq S20	% grid[d]	Γ_{S0} (kcal/mol) eq S22	Γ_{GS} (kcal/mol) eq S24	$\Delta\lambda_0$ (kcal/mol) eq S25	$\Delta\lambda_1$ (kcal/mol) eq S25	$\Delta\Lambda_0$ eq S26	$\Delta\Lambda_1$ eq S26
1	1.0	2.0	2.4	0.95	0.80	0.19	1	0.81
2	0.023	4.0	1.1	0.66	0.58	0.19	1	0.97
3	0.012	6.1	5.1×10^{-3}	4.9×10^{-3}	2.6×10^{-3}	1.7×10^{-3}	1	1
4	3.7×10^{-5}	8.1	2.7×10^{-3}	2.2×10^{-3}	2.0×10^{-4}	1.4×10^{-3}	1	1
5	1.9×10^{-5}	10.0	1.5×10^{-4}	1.5×10^{-4}	3.1×10^{-7}	1.1×10^{-5}	1	1

[a]The first column here represents the number of singular vectors along each dimension $\mathcal{A}$ in the MPS as defined in eq S18 of the Supporting Information. The second column is the product singular value SVR, Ξ_l, defined using eq S20 in the Supporting Information used to truncate the global measure of entanglement. The third column corresponds to the percentage of the overall coupled proton grid (Table 1) needed for the MPS representation of the potential energy surface. The final two columns represent the errors Γ_{S0} and Γ_{GS} in the potential energy surface defined according to eq S22 in Appendix S4. [b]Number of product singular values retained as explained in Section S3, see eq S18. [c]Singular value ratio for the least significant product vector retained in eq S18 as dictated by eq S20. [d]Percentage of the total number of grid points (see Table 1) needed to achieve the accuracy given by Γ_{S0}, Γ_{GS}, $\Delta\lambda_i$, and $\Delta\Lambda_i$.

Table 3. Results for a Potential Energy Surface Where the First Three Dimensions, {R_1, R_2, R_3}, Are Coupled Together

p_1[a]	p_2[a]	$\mathcal{A}$[b]	Ξ_l[c] eq S20	% grid[d]	Γ_{S0} (kcal/mol) eq S22	Γ_{GS} (kcal/mol) eq S24	$\Delta\lambda_0$ (kcal/mol) eq S25	$\Delta\lambda_1$ (kcal/mol) eq S25	$\Delta\Lambda_0$ eq S26	$\Delta\Lambda_1$ eq S26
1	1	1	1.0	0.12	3.4	2.2	2.2	0.72	0.99	0.42
1	2	2	0.017	0.21	2.7	2.1	2.1	0.90	0.99	0.73
1	3	3	8.3×10^{-3}	0.29	2.5	1.5	1.4	0.53	0.99	0.74
2	2	4	8.1×10^{-3}	0.33	0.94	1.1	1.0	0.51	1.0	0.98
3	4	12	2.4×10^{-5}	0.79	0.11	0.085	0.038	0.015	1.0	1.0

[a]The first two columns show the number of singular values along the R_1−R_2 dimensional separation and the R_2−R_3 dimensional separation. This arises due to the sequential bipartite SVD algorithm used here as described in Section S3 and ref 22. [b]Number of product singular values retained as explained in Section S3, see eq S18. [c]Singular value ratio for the least significant product vector retained in eq S18 as dictated by eq S20. [d]Percentage of the total number of grid points (see Table 1) needed to achieve the accuracy given by Γ_{S0}, Γ_{GS}, $\Delta\lambda_i$, and $\Delta\Lambda_i$.

Table 4. Results for the Four-Dimensional Potential Energy Surface[a]

p_1	p_2	p_3	$\mathcal{A}$	Ξ_l eq S20	% grid	Γ_{S0} (kcal/mol) eq S22	Γ_{GS} (kcal/mol) eq S24	$\Delta\lambda_0$ (kcal/mol) eq S25	$\Delta\lambda_1$ (kcal/mol) eq S25	$\Delta\Lambda_0$ eq S26	$\Delta\Lambda_1$ eq S26
1	1	1	1	1	3.0×10^{-3}	3.9	4.9	5.0	3.5	1	0.64
2	4	8	64	6.2×10^{-5}	0.042	2.2	1.4	1.0	1.2	1	0.99
2	5	10	100	3.8×10^{-5}	0.061	2.1	1.7	1.3	0.91	1	0.93
3	19	24	1368	1.0×10^{-4}	0.46	1.1	0.71	0.39	0.22	1	1
3	21	24	1512	1.1×10^{-4}	0.50	0.86	0.46	0.24	0.17	1	1
3	22	24	1584	6.4×10^{-3}	0.53	0.82	0.38	0.18	0.15	1	1
3	29	26	2262	1.0×10^{-5}	0.74	0.75	0.33	0.06	0.056	1	0.99
4	48	30	5760	7.7×10^{-6}	1.4	0.64	0.33	0.12	0.079	1	0.99
5	68	42	14,280	4.5×10^{-6}	2.8	0.35	0.17	0.067	0.064	1	1
10	131	48	62,880	3.1×10^{-15}	6.5	0.23	0.21	0.070	0.052	1	1
20	277	48	265,920	1.5×10^{-16}	16	0.098	0.11	3.5×10^{-3}	8.2×10^{-3}	1	1
24	901	48	1,037,952	7.5×10^{-18}	55	0.020	0.042	7.5×10^{-4}	2.6×10^{-4}	1	1

[a]Here, the columns are similar to those seen in Tables 2 and 3.

produces eigenstates that are exact with three direct product states.

For the three-dimensional system with three shared protons, represented as {R_1, R_2, R_3}, the results for Γ_{S0} and Γ_{GS} can be seen in Table 3. Here, again, less than 1% of the overall grid data is needed to represent the full surface at sub-kJ/mol accuracy. This corresponds to 12 direct product states, that is, $\mathcal{A} = 12$. This result is similar to the results for the two-dimensional, {R_1, R_2}, potential energy surface in Table 2 as it appears as if each singular bond dimension needs three singular vectors to accurately represent the potential energy surface.

The errors for the eigenstates and eigenvalues for the three-dimensional system are shown in the last four columns inside Table 3, and these results are again consistent with the errors in the potential energy surface provided in the same table.

The grid containing four quantum nuclear degrees of freedom, namely, {R_1, R_2, R_3, R_4} in Table 1, appears to require more than three singular values per singular value bond dimension. In Table 4, 1512 direct product states are needed for sub-kcal/mol accuracy over the entire surface, and this result does not follow the previous rate that the two- and three-dimensional potential energy surfaces shared. It appears that the R_4 quantum nuclear degree of freedom increases the global entanglement of the system driving the number of direct product states to increase in the third and fourth singular value bond dimension. This is in part due to an increase in the range sampled by the potential energy surface. This can be seen from Figure 5, where the histograms show the percentage of nuclear geometries present within different potential energy windows. The fraction of configurations with a potential energy of less than 20 kcal/mol from the bottom of the potential is 44% for

https://doi.org/10.1021/acs.jctc.2c00484
J. Chem. Theory Comput. 2022, 18, 7243−7259

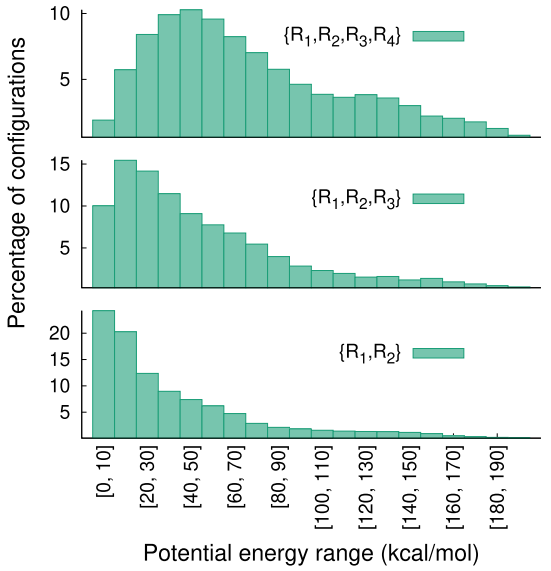

Figure 5. The figure presents the distribution of the water wire configurations according to their potential energy for the two-, three-, and four-dimensional cases. Note that the share of low-energy configurations is decreased significantly as we go higher in dimensionality.

two-dimensional, 25% for three-dimensional, and only 7% for the four-dimensional potential surfaces. Similarly, the fraction of nuclear configurations with potential energy less than 30 kcal/mol is 56% for two-dimensional, 39% for three-dimensional, and 16% for the four-dimensional potential surfaces. Additionally, as seen in Figure 5, the $\{R_1, R_2, R_3, R_4\}$ potential surface occupies a much broader range with a shoulder as far out as 120 kcal/mol above the lowest energy configuration. This signifies that the potential energy increases steeply along the fourth dimension and increases the extent of confinement. The shape of the potential is determined by the donor−acceptor distances. For the water wire system shown in Figure 2a, the donor−acceptor distance for R_4 (3.1 Å) is significantly larger than the donor−acceptor distances for R_1 (2.3 Å), R_2 (2.3 Å), and R_3 (2.4 Å). Hence, the potential energy along R_4 increases steeply as the proton is largely bound to its donor. The computational methods introduced here are sensitive to the levels of details.

For the four-dimensional quantum nuclear degrees of freedom, the potential energy surface must contain more than 1000 direct product states for accurate eigenvectors and eigenvalues. However, these still correspond to less than 1% of the overall multidimensional grid space. Furthermore, the MPS potential energy surface reproduces the ground-state eigenvector with a single direct product state along each of the quantum nuclear degrees of freedom.

In the next section, we inspect the accuracy and efficiency of the propagator, $\exp\{-\iota E_{\mathcal{R},\{\mathcal{G}_\beta\}}(\mathbf{R})t/2\hbar\}$, when the methods presented in the previous sections are used.

4.2. Tensor Network Form of $\exp\{-\iota E_{\mathcal{R},\{\mathcal{G}_\beta\}}(\mathbf{R})t/2\hbar\}$. We next probe the accuracy and efficiency of the representation of the propagator, $\exp\{-\iota E_{\mathcal{R},\{\mathcal{G}_\beta\}}(\mathbf{R})t/2\hbar\}$, discussed above and specifically in eq 5. Again, the same analysis schemes are used as outlined above, where the form of the propagator is studied by incrementally increasing the complexity of the protonated water wire system, one dimension at a time. However, unlike the case of the potential, the value of the time step, t, in eq 5 is critical and is chosen as noted in the captions of Tables 5−7. In general, this critical choice is made during dynamics calculations to keep the error in propagation small. The error in quantum propagation based on eq 3 grows as $O(t^3)$ due to the Trotter factorization of the symmetric split operator.[114−118]

Table 5. Tensor Network Decomposition of $\exp\{-\iota E_{\mathcal{R},\{\mathcal{G}_\beta\}}(\mathbf{R})t/2\hbar\}$ for the Two-Dimensional ($\{R_1, R_2\}$) Case[a]

$\mathcal{A}$	Ξ_l eq S20	% grid	Γ_{fid} eq S27
1	1.0	2.0	0.96
2	0.27	4.0	1.0
3	0.024	6.1	1.0
4	2.5×10^{-3}	8.1	1.0

[a]The time step is chosen to be t = 2.14 fs. The first column is the total number of singular vectors along the two chosen dimensions. The second column is the product singular value ratio (eq S20 in the Supporting Information), followed by the total percentage of the overall grid used to achieve the accuracy shown under Γ_{fid}.

Table 6. Tensor Network Decomposition of $\exp\{-\iota E_{\mathcal{R},\{\mathcal{G}_\beta\}}(\mathbf{R})t/2\hbar\}$ for the $\{R_1, R_2, R_3\}$ Coupled System[a]

p_1[b]	p_2[b]	$\mathcal{A}$[c]	Ξ_l[d] eq S20	% grid[e]	Γ_{fid} eq S27
1	1	1	1.0	0.12	0.98
3	4	12	6.0×10^{-4}	0.79	1.0
3	5	15	6.8×10^{-5}	0.96	1.0
4	7	28	6.3×10^{-7}	1.6	1.0

[a]Here, t = 1.209 fs. The parameters p_1, p_2, $\mathcal{A}$, and Ξ_l are reiterated here for clarity purposes and hold the same meaning as in Table 3. The third column $\mathcal{A}$ refers to the number of product singular values defined in the Supporting Information using eq S12 with errors shown using eqs S20 and S27. [b]Number of product singular values retained as explained in Section S3, see eq S18. [c]Number of product singular values retained as explained in Section S3, see eq S18. [d]Singular value ratio for the least significant product vector retained in eq S18 as dictated by eq S20. [e]Percentage of the total number of grid points (see Table 1) needed to achieve the accuracy given by Γ_{fid}.

Table 7. Tensor Network Decomposition of $\exp\{-\iota E_{\mathcal{R},\{\mathcal{G}_\beta\}}(\mathbf{R})t/2\hbar\}$ for the $\{R_1, R_2, R_3, R_4\}$ Potential Energy Surface[a]

p_1	p_2	p_3	$\mathcal{A}$	Ξ_l eq S20	% grid	Γ_{fid} eq S27
1	1	1	1	1.0	3.4×10^{-3}	0.96
1	3	4	12	0.010	0.017	0.99
1	3	5	15	5.8×10^{-3}	0.020	0.99
3	8	12	288	7.7×10^{-4}	0.11	1.0
3	21	24	1512	3.2×10^{-5}	0.50	1.0
18	133	42	100,548	8.6×10^{-7}	6.8	1.0
24	441	48	508,032	7.2×10^{-18}	27	1.0

[a]Here, t = 1.209 fs. The parameters in the columns retain the same meanings as in Tables 4 and 6.

In Tables 5−7, we present our results. In all cases, we gauge the accuracy using the parameter Γ_{fid} defined using eq S27 inside the Supporting Information. We gauge efficiency using $\mathcal{A}$, which captures the number of direct product states needed to reproduce the propagator at the respective levels of accuracy depicted by Γ_{fid} and the corresponding reduction in grid size associated with use of the product states. In all cases, we find that

https://doi.org/10.1021/acs.jctc.2c00484
J. Chem. Theory Comput. 2022, 18, 7243−7259

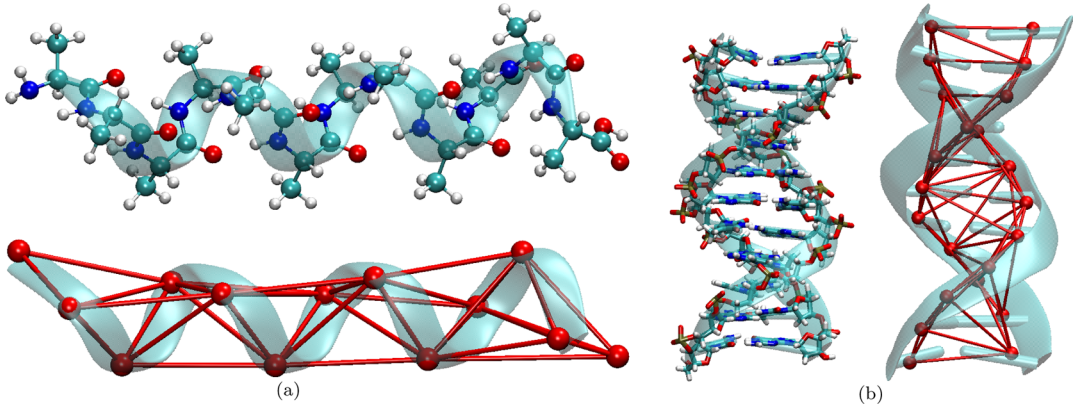

Figure 6. Illustration of the molecular graph and tensor-network decompositions for complex systems.

our results are consistent with those found for the potential. For studies involving dimensions $\{R_1, R_2\}$ and also those involving $\{R_1, R_2, R_3\}$, there are only a few product singular vectors needed, but this value grows sharply upon introduction of R_4 due to the increase in confinement afforded by the larger donor−acceptor distance for R_4 as noted in the previous section. However, even in such cases, our graph-theoretic approach to represent the potential surface and the associated use of tensor networks greatly reduce the amount of data needed to achieve an accurate quantum propagator with little loss in accuracy.

5. CONCLUSIONS

Molecular fragmentation methods have revolutionized quantum chemistry by providing a range of options to obtain accurate post-Hartree−Fock energies, gradients, and other properties at much reduced computational cost, for systems of unprecedented size. The key idea in these methods has been the exploitation of the local correlation properties of molecular systems to only perform steeper scaling calculations in molecular subspaces that need such treatments. Furthermore, when these fragmentation methods are combined with many-body theory and ONIOM, indeed, these lead to a powerful alternative for efficient molecular simulations.

Over a series of publications, we have introduced a graph-theory-based fragmentation procedure that includes within it key elements from many-body approximations and ONIOM. This method has been used to compute accurate post-Hartree−Fock potential surfaces and AIMD trajectories. More recently,[62] these methods have been used to develop novel hybrid quantum-classical algorithms to be implemented on a stream of parallel quantum and classical hardware systems, in a completely asynchronous fashion, to arrive at an efficient, high-fidelity quantum circuit implementation.

In this publication, we take on a very different goal for our graph-theoretic fragmentation procedure. In molecular systems, when quantum nuclear dynamics is needed, an accurate and efficient approximation for the quantum nuclear time-evolution operator is critical. This approach has two parts: one that arises from the free propagator and the other that arises from the exponentiation of a discretized version of the potential energy surface. It is for the latter that we introduce here a novel approximation based on the graph-theoretic molecular fragmentation approximation to the potential energy surface. In doing so, we find that the application of the new approximation to the exponential of the potential on some initial wavepacket automatically results in a tensor network form that enormously reduces the associated exponential computational complexity present within quantum nuclear dynamics. We demonstrate the method by computing potential surfaces and the exponential, time-evolution form of the same for a range of protonated water wire systems and find that the method accurately represents these at much reduced computational cost and reduced data storage. We also show how this approach can be extended to more complex systems. However, critical challenges remain. Although our approach allows for retention of long-range electron correlation effects to be included at some low level of electronic structure theory (such as DFT-B3LYP for the cases studied here) within the quantum nuclear dynamics description, certainly, the non-classical long-range order, which is the result of long-range correlation, would be absent when smaller values of $\mathcal{R}$ are used in our formalism. It remains to be seen how effectively larger values of $\mathcal{R}$ can reproduce true long-range electron correlation (and associated coupling with nuclear quantization as represented within the current tensor-network approach). However, in such cases, our approach will allow a systematic procedure to improve the approximation by gradually increasing $\mathcal{R}$ and also the edge-length cutoff criterion, to systematically improve results.

APPENDIX A

Molecular Graph and Tensor-Network Representations for More Complex Systems

The molecular graph representations for a protonated water wire system are provided in the main text of the paper. Here, we present two additional discussions for a 3_{10}-helix (Figure 6a) and DNA (Figure 6b) fragmentation to showcase the generality of the graph-theoretic approach. Our graph-based fragmentation is general, and the electronic structure aspects have been discussed in refs 46, 49−57, 62, and 63. To help clarify, we present two illustrations in Figure 6, which show how the graph partition is done for more complex systems that may also display quantum nuclear effects. In Figure 6a, we show a 3_{10}-helix, which is stabilized by hydrogen bonds, and similarly in Figure 6b, a DNA double helix is also stabilized by hydrogen bonds. First, we explain how the graphs are obtained for these systems, and then, we show how tensor networks may be written if the shared protons in the hydrogen bonds are to be treated quantum mechanically (while our discussion here assumes nuclear quantum effects from shared protons, this is not a limitation in the method. One may generalize this to arbitrary quantum nuclear dimensions, but the numerical demonstration of this aspect is not considered here).

https://doi.org/10.1021/acs.jctc.2c00484
J. Chem. Theory Comput. 2022, 18, 7243−7259

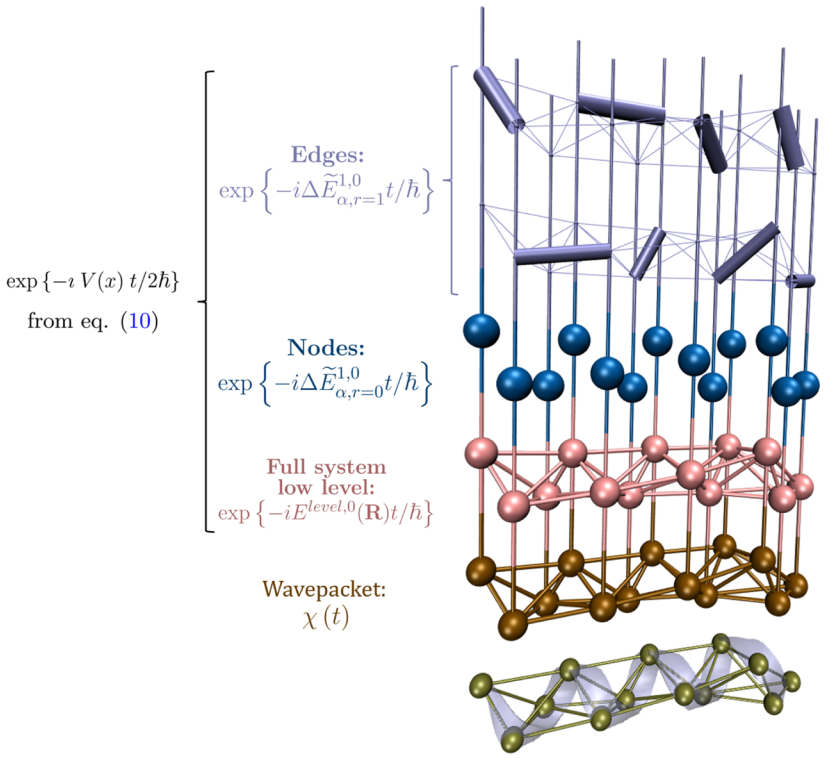

Figure 7. Similar to Figure 3 but now the tensor network formalism is applied to the graphical depiction in Figure 6a. Note that the bottom figure here is the same as the graphical rendering in Figure 6a.

Our code for obtaining the graphs (and hence fragments that are denoted by the simplexes) is general and allows for arbitrary graph formation, based on the needed (local and nonuniform) many-body interactions. The system in Figure 6a was used in ref 52. For the electronic structure portion, the graph is first generated by defining a set of nodes which represent coarse-grained molecular units such as water, hydronium, a single amino acid, and so forth. Next, an upper limit to the spatial extent of two-body interactions is specified which helps determine edges and thus the graph. For example, in Figure 6a, the nodes are amino acid monomers, whereas the edges include all interactions between an amino acid monomer and monomers in a neighboring helical turn. Our Python-based code then generates all fragments up to a maximum rank $\mathcal{R}$ specified by the user. Furthermore, now the computation of $E^{level,1}_{\alpha,r}(\mathbf{R}_{\alpha,r})$ and $E^{level,0}_{\alpha,r}(\mathbf{R}_{\alpha,r})$ in eqs 1 and 2 is completely independent, and hence, the associated electronic structure calculations are spawned in an asynchronous manner. The potential surface is generated in a similar manner by considering a collection of simplexes (or fragments) that capture all the needed many-body interactions, triggered by a general graph formalism.[46,54,57]

When quantum nuclear effects are needed, the current paper derives tensor networks from the above-mentioned graph decomposition, and eqs 4 and 5 represent the most general expression for the resulting action, which applies to all graph structures. However, in such general situations, the appropriate tensor network topology may be more complicated and may not in general have an MPS form if one were to consider the most significant correlations. This can readily be seen from Figure 7 which represents a natural generalization of Figure 3, except now the tensor network formalism (eqs 4 and 5) is applied to the graphical depiction in Figure 6a. Thus, the bottom layer of Figure 7 represents the graphical depiction in Figure 6a. Following this, the brown layer in Figure 7 represents the tensor network depiction of the quantum nuclear wavepacket. That is, the initial nuclear wavepacket now has a more general form than that in eq 8, in that each tensor core that represents the nuclear degrees of freedom within one node is connected now based on the graph structure of the molecular system. The potential propagator however retains its general form in eqs 4 and 5 and hence can still be applied to this more general initial wavepacket. As a result, the action of the nodal portions ($\mathbf{V}_0$ terms in eq 5) is represented using the dark-blue spheres in Figure 7, whereas the edge portions are represented using the light-blue rods in Figure 7. We compare these with the appropriate portions of Figure 3. The full system low level (first term on the right side of eq 4) is represented in pink in Figure 7 and retains the same structure as that of the original graph.

Although clearly, the general situation may warrant initial wavepackets that are not MPS states, the structure of eqs 4 and 5 retains its general form. Even so, if needed, an MPS can always be constructed for any rank-$\mathcal{N}$ tensor. The only question is whether it has the maximum compression of data based on graph topologies such as those shown here. Although the expressions provided in the paper are general and will still apply to arbitrary tensor-network input states, numerical implementation of the same will be reserved for a future publication. Furthermore, whether such general TN states need to be considered or not for any given problem would be a choice based on efficiency versus accuracy. Although on the one end, the MPS form may be easier to handle, more general TN forms such as those in Figure 7 may appropriately capture the molecular correlations. In such situations, for example, the MPS may need more bond dimensions for the full system low level for accurate simulations. Additionally, as seen in Figure 6b, the quantum nuclear degrees of freedom encompassed within a node are correlated to several other nodes (through edges and faces), but the resultant propagator is still of the same product form as that in eqs 4 and 5.

https://doi.org/10.1021/acs.jctc.2c00484
J. Chem. Theory Comput. 2022, 18, 7243−7259

Although our propagation code is written in a general way to handle such situations, it is still sensitive to the choice of the initial wavepacket (i.e., MPS or not), and numerical testing is essential in such cases. This paper numerically illustrates our work for an MPS input state.

■ ASSOCIATED CONTENT

Supporting Information

The Supporting Information is available free of charge at https://pubs.acs.org/doi/10.1021/acs.jctc.2c00484.

Sequential bipartite Schmidt decomposition, matrix product states, gauging correlations in the MPS, and gauging accuracy of the tensor network form (PDF)

■ AUTHOR INFORMATION

Corresponding Author

Srinivasan S. Iyengar − *Department of Chemistry, and the Indiana University Quantum Science and Engineering Center (IU-QSEC), Indiana University, Bloomington, Indiana 47405, United States;* orcid.org/0000-0001-6526-2907; Email: iyengar@indiana.edu

Authors

Anup Kumar − *Department of Chemistry, and the Indiana University Quantum Science and Engineering Center (IU-QSEC), Indiana University, Bloomington, Indiana 47405, United States*

Nicole DeGregorio − *Department of Chemistry, and the Indiana University Quantum Science and Engineering Center (IU-QSEC), Indiana University, Bloomington, Indiana 47405, United States*

Timothy Ricard − *Department of Chemistry, and the Indiana University Quantum Science and Engineering Center (IU-QSEC), Indiana University, Bloomington, Indiana 47405, United States*

Complete contact information is available at: https://pubs.acs.org/10.1021/acs.jctc.2c00484

Notes

The authors declare no competing financial interest.

■ ACKNOWLEDGMENTS

This research was supported by the National Science Foundation grants CHE-2102610 to author S.S.I.

■ REFERENCES

(1) *Hydrogen-Transfer Reactions*; Hynes, J. T., Klinman, J. P., Limbach, H.-H., Schowen, R. L., Eds.; Wiley-VCH: Weinheim, Germany, 2007.

(2) Klinman, J. P. Dynamically Achieved Active Site Precision in Enzyme Catalysis. *Acc. Chem. Res.* **2015**, *48*, 449−456.

(3) Hammes-Schiffer, S. Theory of Proton-Coupled Electron Transfer in Energy Conversion Processes. *Acc. Chem. Res.* **2009**, *42*, 1881−1889.

(4) Nagel, Z.; Klinman, J. Tunneling and Dynamics in Enzymatic Hydride Transfer. *Chem. Rev.* **2006**, *106*, 3095.

(5) Soudackov, A. V.; Hammes-Schiffer, S. Probing Nonadiabaticity in the Proton-Coupled Electron Transfer Reaction Catalyzed by Soybean Lipoxygenase. *J. Phys. Chem. Lett.* **2014**, *5*, 3274.

(6) Cukier, R. I.; Nocera, D. G. Proton-coupled electron transfer. *Annu. Rev. Phys. Chem.* **1998**, *49*, 337−369.

(7) Mayer, J. M. PROTON-COUPLED ELECTRON TRANSFER: A Reaction Chemist's View. *Annu. Rev. Phys. Chem.* **2004**, *55*, 363−390.

(8) Iyengar, S. S.; Sumner, I.; Jakowski, J. Hydrogen Tunneling in an Enzyme Active Site: A Quantum Wavepacket Dynamical Perspective. *J. Phys. Chem. B* **2008**, *112*, 7601.

(9) Sumner, I.; Iyengar, S. S. Analysis of Hydrogen Tunneling in an Enzyme Active Site Using Von Neumann Measurements. *J. Chem. Theory Comput.* **2010**, *6*, 1698.

(10) Deumens, E.; Diz, A.; Longo, R.; Öhrn, Y. Time-dependent theoretical treatments of the dynamics of electrons and nuclei in molecular systems. *Rev. Mod. Phys.* **1994**, *66*, 917.

(11) Raghavachari, K.; Trucks, G. W.; Pople, J. A.; Head-Gordon, M. A fifth-order perturbation comparison of electron correlation theories. *Chem. Phys. Lett.* **1989**, *157*, 479−483.

(12) Feynman, R. P.; Hibbs, A. R. *Quantum Mechanics and Path Integrals*; McGraw-Hill Book Company: New York, 1965.

(13) Meyer, H.-D.; Manthe, U.; Cederbaum, L. S. The Multi-Configurational Time-Dependent Hartree Approach. *Chem. Phys. Lett.* **1990**, *165*, 73.

(14) Nielsen, M. A.; Chuang, I. L. *Quantum Computation and Quantum Information*; Cambridge University Press: Cambridge, 2000.

(15) Feynman, R. P.; Hey, J.; Allen, R. W. *Feynman Lectures on Computation*; Addison-Wesley Longman Publishing Co., Inc., 1998.

(16) Jakowski, J.; Sumner, I.; Iyengar, S. S. Computational Improvements to Quantum Wave Packet ab Initio Molecular Dynamics Using a Potential-Adapted, Time-Dependent Deterministic Sampling Technique. *J. Chem. Theory Comput.* **2006**, *2*, 1203.

(17) Sumner, I.; Iyengar, S. S. Quantum Wavepacket Ab Initio Molecular Dynamics: An Approach for Computing Dynamically Averaged Vibrational Spectra Including Critical Nuclear Quantum Effects. *J. Phys. Chem. A* **2007**, *111*, 10313.

(18) Braams, B. J.; Bowman, J. M. Permutationally invariant potential energy surfaces in high dimensionality. *Int. Rev. Phys. Chem.* **2009**, *28*, 577.

(19) Hocker, D.; Li, X.; Iyengar, S. S. Shannon Entropy Based Time-Dependent Deterministic Sampling for Efficient "On-the-Fly" Quantum Dynamics and Electronic Structure. *J. Chem. Theory Comput.* **2011**, *7*, 256.

(20) Peláez, D.; Meyer, H.-D. The multigrid POTFIT (MGPF) method: Grid representations of potentials for quantum dynamics of large systems. *J. Chem. Phys.* **2013**, *138*, 014108.

(21) DeGregorio, N.; Iyengar, S. S. Efficient and Adaptive Methods for Computing Accurate Potential Surfaces for Quantum Nuclear Effects: Applications to Hydrogen-Transfer Reactions. *J. Chem. Theory Comput.* **2018**, *14*, 30−47.

(22) DeGregorio, N.; Iyengar, S. S. Adaptive Dimensional Decoupling for Compression of Quantum Nuclear Wave Functions and Efficient Potential Energy Surface Representations through Tensor Network Decomposition. *J. Chem. Theory Comput.* **2019**, *15*, 2780.

(23) Hackbusch, W.; Khoromskij, B. N. Tensor-product approximation to operators and functions in high dimensions. *J. Complexity* **2007**, *23*, 697−714.

(24) Greene, S. M.; Batista, V. S. Tensor-Train Split-Operator Fourier Transform (TT-SOFT) Method: Multidimensional Nonadiabatic Quantum Dynamics. *J. Chem. Theory Comput.* **2017**, *13*, 4034−4042.

(25) Orús, R. A practical introduction to tensor networks: Matrix product states and projected entangled pair states. *Ann. Phys.* **2014**, *349*, 117−158.

(26) Wang, H.; Thoss, M. Multilayer formulation of the multi-configuration time-dependent Hartree theory. *J. Chem. Phys.* **2003**, *119*, 1289−1299.

(27) Kassal, I.; Jordan, S. P.; Love, P. J.; Mohseni, M.; Aspuru-Guzik, A. Polynomial-time quantum algorithm for the simulation of chemical dynamics. *Proc. Natl. Acad. Sci. U.S.A.* **2008**, *105*, 18681−18686.

(28) MacDonell, R. J.; Dickerson, C. E.; Birch, C. J.; Kumar, A.; Edmunds, C. L.; Biercuk, M. J.; Hempel, C.; Kassal, I. Analog quantum simulation of chemical dynamics. *Chem. Sci.* **2021**, *12*, 9794−9805.

(29) Ollitrault, P. J.; Baiardi, A.; Reiher, M.; Tavernelli, I. Hardware efficient quantum algorithms for vibrational structure calculations. *Chem. Sci.* **2020**, *11*, 6842−6855.

(30) Sawaya, N. P. D.; Menke, T.; Kyaw, T. H.; Johri, S.; Aspuru-Guzik, A.; Guerreschi, G. G. Resource-efficient digital quantum simulation of d-level systems for photonic, vibrational, and spin-s Hamiltonians. *npj Quantum Inf.* **2020**, *6*, 49.

(31) Teplukhin, A.; Kendrick, B. K.; Babikov, D. Solving complex eigenvalue problems on a quantum annealer with applications to quantum scattering resonances. *Phys. Chem. Chem. Phys.* **2020**, *22*, 26136−26144.
(32) Jahangiri, S.; Arrazola, J. M.; Quesada, N.; Delgado, A. Quantum algorithm for simulating molecular vibrational excitations. *Phys. Chem. Chem. Phys.* **2020**, *22*, 25528−25537.
(33) Wang, C. S.; Curtis, J. C.; Lester, B. J.; Zhang, Y.; Gao, Y. Y.; Freeze, J.; Batista, V. S.; Vaccaro, P. H.; Chuang, I. L.; Frunzio, L.; Jiang, L.; Girvin, S. M.; Schoelkopf, R. J. Efficient Multiphoton Sampling of Molecular Vibronic Spectra on a Superconducting Bosonic Processor. *Phys. Rev. X* **2020**, *10*, 021060.
(34) Saha, D.; Iyengar, S. S.; Richerme, P.; Smith, J. M.; Sabry, A. Mapping Quantum Chemical Dynamics Problems to Spin-Lattice Simulators. *J. Chem. Theory Comput.* **2021**, *17*, 6713−6732.
(35) Peruzzo, A.; McClean, J.; Shadbolt, P.; Yung, M.-H.; Zhou, X.-Q.; Love, P. J.; Aspuru-Guzik, A.; O'Brien, J. L. A variational eigenvalue solver on a photonic quantum processor. *Nat. Commun.* **2014**, *5*, 4213.
(36) Kandala, A.; Mezzacapo, A.; Temme, K.; Takita, M.; Brink, M.; Chow, J. M.; Gambetta, J. M. Hardware-efficient variational quantum eigensolver for small molecules and quantum magnets. *Nature* **2017**, *549*, 242.
(37) O'Malley, P. J. J.; Babbush, R.; Kivlichan, I. D.; Romero, J.; McClean, J. R.; Barends, R.; Kelly, J.; Roushan, P.; Tranter, A.; Ding, N.; Campbell, B.; Chen, Y.; Chen, Z.; Chiaro, B.; Dunsworth, A.; Fowler, A. G.; Jeffrey, E.; Lucero, E.; Megrant, A.; Mutus, J. Y.; Neeley, M.; Neill, C.; Quintana, C.; Sank, D.; Vainsencher, A.; Wenner, J.; White, T. C.; Coveney, P. V.; Love, P. J.; Neven, H.; Aspuru-Guzik, A.; Martinis, J. M. Scalable Quantum Simulation of Molecular Energies. *Phys. Rev. X* **2016**, *6*, 031007.
(38) Grimsley, H. R.; Economou, S. E.; Barnes, E.; Mayhall, N. J. An adaptive variational algorithm for exact molecular simulations on a quantum computer. *Nat. Commun.* **2019**, *10*, 3007.
(39) Nam, Y.; Chen, J.-S.; Pisenti, N. C.; Wright, K.; Delaney, C.; Maslov, D.; Brown, K. R.; Allen, S.; Amini, J. M.; Apisdorf, J.; Beck, K. M.; Blinov, A.; Chaplin, V.; Chmielewski, M.; Collins, C.; Debnath, S.; Hudek, K. M.; Ducore, A. M.; Keesan, M.; Kreikemeier, S. M.; Mizrahi, J.; Solomon, P.; Williams, M.; Wong-Campos, J. D.; Moehring, D.; Monroe, C.; Kim, J. Ground-state energy estimation of the water molecule on a trapped-ion quantum computer. *npj Quantum Inf.* **2020**, *6*, 33.
(40) Zhang, D.-B.; Yuan, Z.-H.; Yin, T. *Variational Quantum Eigensolvers by Variance Minimization*, 2020. arXiv preprint arXiv:2006.15781.
(41) Parrish, R. M.; Hohenstein, E. G.; McMahon, P. L.; Martínez, T. J. Quantum Computation of Electronic Transitions Using a Variational Quantum Eigensolver. *Phys. Rev. Lett.* **2019**, *122*, 230401.
(42) Shen, Y.; Zhang, X.; Zhang, S.; Zhang, J.-N.; Yung, M.-H.; Kim, K. Quantum implementation of the unitary coupled cluster for simulating molecular electronic structure. *Phys. Rev. A* **2017**, *95*, 020501.
(43) Xia, R.; Kais, S. Quantum machine learning for electronic structure calculations. *Nat. Commun.* **2018**, *9*, 4195.
(44) Grimsley, H. R.; Claudino, D.; Economou, S. E.; Barnes, E.; Mayhall, N. J. Is the Trotterized UCCSD Ansatz Chemically Well-Defined? *J. Chem. Theory Comput.* **2019**, *16*, 1−6.
(45) Tilly, J.; Jones, G.; Chen, H.; Wossnig, L.; Grant, E. Computation of molecular excited states on IBM quantum computers using a discriminative variational quantum eigensolver. *Phys. Rev. A* **2020**, *102*, 062425.
(46) Kumar, A.; DeGregorio, N.; Iyengar, S. S. Graph-Theory-Based Molecular Fragmentation for Efficient and Accurate Potential Surface Calculations in Multiple Dimensions. *J. Chem. Theory Comput.* **2021**, *17*, 6671−6690.
(47) Yang, B.; Zhang, P.; Qu, C.; Wang, X. H.; Stancil, P. C.; Bowman, J. M.; Balakrishnan, N.; McLaughlin, B. M.; Forrey, R. C. Full-Dimensional Quantum Dynamics of SiO in Collision with H2. *J. Phys. Chem. A* **2018**, *122*, 1511−1520.
(48) Qu, C.; Conte, R.; Houston, P. L.; Bowman, J. M. Full-dimensional potential energy surface for acetylacetone and tunneling splittings. *Phys. Chem. Chem. Phys.* **2021**, *23*, 7758−7767.
(49) Li, J.; Iyengar, S. S. Ab Initio Molecular Dynamics Using Recursive, Spatially Separated, Overlapping Model Subsystems Mixed within an ONIOM-Based Fragmentation Energy Extrapolation Technique. *J. Chem. Theory Comput.* **2015**, *11*, 3978−3991.
(50) Li, J.; Haycraft, C.; Iyengar, S. S. Hybrid Extended Lagrangian, Post-Hartree-Fock Born-Oppenheimer ab Initio Molecular Dynamics Using Fragment-Based Electronic Structure. *J. Chem. Theory Comput.* **2016**, *12*, 2493.
(51) Haycraft, C.; Li, J.; Iyengar, S. S. Efficient, "On-the-fly" Born−Oppenheimer and Car−Parrinello−type Dynamics with coupled cluster accuracy through Fragment Based Electronic Structure. *J. Chem. Theory Comput.* **2017**, *13*, 1887.
(52) Ricard, T. C.; Haycraft, C.; Iyengar, S. S. Adaptive, geometric networks for efficient coarse-grained ab initio molecular dynamics with post-Hartree-Fock accuracy. *J. Chem. Theory Comput.* **2018**, *14*, 2852.
(53) Ricard, T. C.; Iyengar, S. S. Efficiently Capturing Weak Interactions in ab Initio Molecular Dynamics with on-the-Fly Basis Set Extrapolation. *J. Chem. Theory Comput.* **2018**, *14*, 5535.
(54) Kumar, A.; Iyengar, S. S. Fragment-based electronic structure for potential energy surfaces using a superposition of fragmentation topologies. *J. Chem. Theory Comput.* **2019**, *15*, 5769.
(55) Ricard, T. C.; Kumar, A.; Iyengar, S. S. Embedded, graph-theoretically defined many-body approximations for wavefunction-in-DFT and DFT-in-DFT: Applications to gas- and condensed-phase ab initio molecular dynamics, and potential surfaces for quantum nuclear effects. *Int. J. Quantum Chem.* **2020**, *120*, No. e26244.
(56) Ricard, T. C.; Iyengar, S. S. Efficient and Accurate Approach To Estimate Hybrid Functional and Large Basis-Set Contributions to Condensed-Phase Systems and Molecule-Surface Interactions. *J. Chem. Theory Comput.* **2020**, *16*, 4790.
(57) Zhang, J. H.; Ricard, T. C.; Haycraft, C.; Iyengar, S. S. Weighted-Graph-Theoretic Methods for Many-Body Corrections within ONIOM: Smooth AIMD and the Role of High-Order Many-Body Terms. *J. Chem. Theory Comput.* **2021**, *17*, 2672−2690.
(58) Ayral, T.; Le Régent, F.-M.; Saleem, Z.; Alexeev, Y.; Suchara, M. Quantum Divide and Compute: Hardware Demonstrations and Noisy Simulations. In *2020 IEEE Computer Society Annual Symposium on VLSI (ISVLSI)*, 2020; pp 138−140. DOI: 10.1109/isvlsi49217.2020.00034
(59) Peng, T.; Harrow, A. W.; Ozols, M.; Wu, X. Simulating Large Quantum Circuits on a Small Quantum Computer. *Phys. Rev. Lett.* **2020**, *125*, 150504.
(60) Perlin, M. A.; Saleem, Z. H.; Suchara, M.; Osborn, J. C. Quantum circuit cutting with maximum-likelihood tomography. *npj Quantum Inf.* **2021**, *7*, 64.
(61) Tang, W.; Tomesh, T.; Suchara, M.; Larson, J.; Martonosi, M. CutQC: Using Small Quantum Computers for Large Quantum Circuit Evaluations. In *Proceedings of the 26th ACM International Conference on Architectural Support for Programming Languages and Operating Systems*; Association for Computing Machinery, 2021; pp 473−486. DOI: 10.1145/3445814.3446758
(62) Zhang, J. H.; Iyengar, S. S. Graph-$|Q\rangle\langle C|$, a Graph-Based Quantum/Classical Algorithm for Efficient Electronic Structure on Hybrid Quantum/Classical Hardware Systems: Improved Quantum Circuit Depth Performance. *J. Chem. Theory Comput.* **2022**, *18*, 2885.
(63) Zhu, X.; Iyengar, S. S. Graph Theoretic Molecular Fragmentation for Multidimensional Potential Energy Surfaces Yield an Adaptive and General Transfer Machine Learning Protocol. *J. Chem. Theory Comput.* **2022**, *18*, 5125−5144.
(64) Zhang, D. W.; Zhang, J. Z. H. Molecular fractionation with conjugate caps for full quantum mechanical calculation of protein-molecule interaction energy. *J. Chem. Phys.* **2003**, *119*, 3599.
(65) Hopkins, B. W.; Tschumper, G. S. Multicentred QM/QM Methods for Overlapping Model Systems. *Mol. Phys.* **2005**, *103*, 309.
(66) Stoll, H.; Paulus, B.; Fulde, P. On the accuracy of correlation-energy expansions in terms of local increments. *J. Chem. Phys.* **2005**, *123*, 144108.

(67) Huang, L.; Massa, L.; Karle, J. Kernel energy method: Application to DNA. *Biochem* **2005**, *44*, 16747.
(68) Ganesh, V.; Dongare, R. K.; Balanarayan, P.; Gadre, S. R. Molecular Tailoring Approach for Geometry Optimization of Large Molecules: Energy Evaluation and Parallelization Strategies. *J. Chem. Phys.* **2006**, *125*, 104109.
(69) Guo, W.; Wu, A.; Xu, X. XO: An extended ONIOM method for accurate and efficient geometry optimization of large molecules. *Chem. Phys. Lett.* **2010**, *498*, 203−208.
(70) Jacobson, L. D.; Herbert, J. M. An Efficient, Fragment-Based Electronic Structure Method for Molecular Systems: Self-Consistent Polarization with Perturbative Two-Body Exchange and Dispersion. *J. Chem. Phys.* **2011**, *134*, 094118.
(71) Richard, R. M.; Herbert, J. M. A Generalized Many-Body Expansion and a Unified View of Fragment-Based Methods in Electronic Structure Theory. *J. Chem. Phys.* **2012**, *137*, 064113.
(72) Le, H.-A.; Tan, H.-J.; Ouyang, J. F.; Bettens, R. P. A. Combined Fragmentation Method: A Simple Method for Fragmentation of Large Molecules. *J. Chem. Theory Comput.* **2012**, *8*, 469.
(73) Li, S.; Li, W.; Ma, J. Generalized Energy-Based Fragmentation Approach and Its Applications to Macromolecules and Molecular Aggregates. *Acc. Chem. Res.* **2014**, *47*, 2712.
(74) Gordon, M.; Mullin, J.; Pruitt, S.; Roskop, L.; Slipchenko, L.; Boatz, J. Accurate Methods for Large Molecular Systems. *J. Phys. Chem. B* **2009**, *113*, 9646.
(75) Raghavachari, K.; Saha, A. Accurate Composite and Fragment-Based Quantum Chemical Models for Large Molecules. *Chem. Rev.* **2015**, *115*, 5643.
(76) Collins, M. A.; Bettens, R. P. A. Energy-Based Molecular Fragmentation Methods. *Chem. Rev.* **2015**, *115*, 5607.
(77) Collins, M. A. Systematic Fragmentation of Large Molecules by Annihilation. *Phys. Chem. Chem. Phys.* **2012**, *14*, 7744.
(78) Willow, S. Y.; Salim, M. A.; Kim, K. S.; Hirata, S. Ab initio molecular dynamics of liquid water using embedded-fragment second-order many-body perturbation theory towards its accurate property prediction. *Sci. Rep.* **2015**, *5*, 14358.
(79) Han, J.; Mazack, M. J.; Zhang, P.; Truhlar, D. G.; Gao, J. Quantum mechanical force field for water with explicit electronic polarization. *J. Chem. Phys.* **2013**, *139*, 054503.
(80) Beran, G. J. Modeling polymorphic molecular crystals with electronic structure theory. *Chem. Rev.* **2016**, *116*, 5567.
(81) Beran, G. J. O.; Nanda, K. Predicting Organic Crystal Lattice Energies with Chemical Accuracy. *J. Phys. Chem. Lett.* **2010**, *1*, 3480−3487.
(82) Bates, D. M.; Smith, J. R.; Janowski, T.; Tschumper, G. S. Development of a 3-body:many-body integrated fragmentation method for weakly bound clusters and application to water clusters (H2O)n= 3 − 10, 16, 17. *J. Chem. Phys.* **2011**, *135*, 044123.
(83) Liu, J.; Qi, L.-W.; Zhang, J. Z. H.; He, X. Fragment Quantum Mechanical Method for Large-Sized Ion-Water Clusters. *J. Chem. Theory Comput.* **2017**, *13*, 2021.
(84) Herbert, J. M. Fantasy versus reality in fragment-based quantum chemistry. *J. Chem. Phys.* **2019**, *151*, 170901.
(85) Varandas, A. J.; Murrell, J. N. A many-body expansion of polyatomic potential energy surfaces: application to H n systems. *Faraday Discuss. Chem. Soc.* **1977**, *62*, 92.
(86) Murrell, J.; Carter, S.; Farantos, S.; Huxley, P.; Varandas, A. *Molecular Potential Energy Functions*; Wiley: New York, 1984.
(87) Varandas, A. J.; Brown, F. B.; Mead, C. A.; Truhlar, D. G.; Blais, N. C. A double many-body expansion of the two lowest-energy potential surfaces and nonadiabatic coupling for H3. *J. Chem. Phys.* **1987**, *86*, 6258−6269.
(88) Varandas, A.; Pais, A. A realistic double many-body expansion (DMBE) potential energy surface for ground-state O3from a multiproperty fit toab initiocalculations, and to experimental spectroscopic, inelastic scattering, and kinetic isotope thermal rate data. *Mol. Phys.* **1988**, *65*, 843.
(89) Lynch, G. C.; Steckler, R.; Schwenke, D. W.; Varandas, A. J. C.; Truhlar, D. G.; Garrett, B. C. Use of scaled external correlation, a double many-body expansion, and variational transition state theory to calibrate a potential energy surface for FH2. *J. Chem. Phys.* **1991**, *94*, 7136−7149.
(90) Xantheas, S. S. Ab Initio Studies of Cyclic Water Clusters $(H_2O)_n$, N=1−6. II. Analysis of Many-body Interactions. *J. Chem. Phys.* **1994**, *100*, 7523.
(91) Dahlke, E. E.; Truhlar, D. G. Electrostatically Embedded Many-Body Expansion for Large Systems, with Applications to Water Clusters. *J. Chem. Theory Comput.* **2007**, *3*, 46.
(92) Hirata, S. Fast electron-correlation methods for molecular crystals: An application to the α, β1, and β2 modifications of solid formic acid. *J. Chem. Phys.* **2008**, *129*, 204104.
(93) Bygrave, P. J.; Allan, N. L.; Manby, F. R. The embedded many-body expansion for energetics of molecular crystals. *J. Chem. Phys.* **2012**, *137*, 164102.
(94) Yang, J.; Hu, W.; Usvyat, D.; Matthews, D.; Schütz, M.; Chan, G. K.-L. Ab initio determination of the crystalline benzene lattice energy to sub-kilojoule/mole accuracy. *Science* **2014**, *345*, 640.
(95) Cisneros, G. A.; Wikfeldt, K. T.; Ojamäe, L.; Lu, J.; Xu, Y.; Torabifard, H.; Bartók, A. P.; Csányi, G.; Molinero, V.; Paesani, F. Modeling Molecular Interactions in Water: From Pairwise to Many-Body Potential Energy Functions. *Chem. Rev.* **2016**, *116*, 7501.
(96) Demerdash, O.; Mao, Y.; Liu, T.; Head-Gordon, M.; Head-Gordon, T. Assessing many-body contributions to intermolecular interactions of the AMOEBA force field using energy decomposition analysis of electronic structure calculations. *J. Chem. Phys.* **2017**, *147*, 161721.
(97) Yu, Q.; Bowman, J. M. Communication: VSCF/VCI vibrational spectroscopy of H_7O3+ and H_9O4+ using high-level, many-body potential energy surface and dipole moment surfaces. *J. Chem. Phys.* **2017**, *146*, 121102.
(98) Yao, K.; Herr, J. E.; Parkhill, J. The many-body expansion combined with neural networks. *J. Chem. Phys.* **2017**, *146*, 014106.
(99) Maseras, F.; Morokuma, K. IMOMM: A new integratedab initio + molecular mechanics geometry optimization scheme of equilibrium structures and transition states. *J. Comput. Chem.* **1995**, *16*, 1170.
(100) Svensson, M.; Humbel, S.; Froese, R. D.; Matsubara, T.; Sieber, S.; Morokuma, K. ONIOM: a multilayered integrated MO + MM method for geometry optimizations and single point energy predictions. A test for Diels-Alder reactions and $Pt(P(t\text{-}Bu)_3)_2 + H_2$ oxidative addition. *J. Phys. Chem.* **1996**, *100*, 19357.
(101) Kerdcharoen, T.; Morokuma, K. ONIOM-XS: an extension of the ONIOM method for molecular simulation in condensed phase. *Chem. Phys. Lett.* **2002**, *355*, 257.
(102) Chung, L. W.; Hirao, H.; Li, X.; Morokuma, K. The ONIOM Method: Its Foundation and Applications to Metalloenzymes and Photobiology. *Wiley Interdiscip. Rev.: Comput. Mol. Sci.* **2012**, *2*, 327.
(103) Chung, L. W.; Sameera, W. M. C.; Ramozzi, R.; Page, A. J.; Hatanaka, M.; Petrova, G. P.; Harris, T. V.; Li, X.; Ke, Z.; Liu, F.; Li, H.-B.; Ding, L.; Morokuma, K. The ONIOM Method and Its Applications. *Chem. Rev.* **2015**, *115*, 5678.
(104) Frisch, M. J.; Trucks, G. W.; Schlegel, H. B.; Scuseria, G. E.; Robb, M. A.; Cheeseman, J. R.; Scalmani, G.; Barone, V.; Petersson, G. A.; Nakatsuji, H.; Li, X.; Caricato, M.; Marenich, A. V.; Bloino, J.; Janesko, B. G.; Gomperts, R.; Mennucci, B.; Hratchian, H. P.; Ortiz, J. V.; Izmaylov, A. F.; Sonnenberg, J. L.; Williams-Young, D.; Ding, F.; Lipparini, F.; Egidi, F.; Goings, J.; Peng, B.; Petrone, A.; Henderson, T.; Ranasinghe, D.; Zakrzewski, V. G.; Gao, J.; Rega, N.; Zheng, G.; Liang, W.; Hada, M.; Ehara, M.; Toyota, K.; Fukuda, R.; Hasegawa, J.; Ishida, M.; Nakajima, T.; Honda, Y.; Kitao, O.; Nakai, H.; Vreven, T.; Throssell, K.; Montgomery, J. A., Jr.; Peralta, J. E.; Ogliaro, F.; Bearpark, M. J.; Heyd, J. J.; Brothers, E. N.; Kudin, K. N.; Staroverov, V. N.; Keith, T. A.; Kobayashi, R.; Normand, J.; Raghavachari, K.; Rendell, A. P.; Burant, J. C.; Iyengar, S. S.; Tomasi, J.; Cossi, M.; Millam, J. M.; Klene, M.; Adamo, C.; Cammi, R.; Ochterski, J. W.; Martin, R. L.; Morokuma, K.; Farkas, O.; Foresman, J. B.; Fox, D. J. *Gaussian 16 Revision B.01*; Gaussian Inc: Wallingford CT, 2016.
(105) Neese, F. The ORCA program system. *Wiley Interdiscip. Rev.: Comput. Mol. Sci.* **2012**, *2*, 73.

https://doi.org/10.1021/acs.jctc.2c00484
J. Chem. Theory Comput. 2022, 18, 7243−7259

(106) Parrish, R. M.; Burns, L. A.; Smith, D. G. A.; Simmonett, A. C.; DePrince, A. E., III; Hohenstein, E. G.; Bozkaya, U.; Sokolov, A. Y.; Di Remigio, R.; Richard, R. M.; Gonthier, J. F.; James, A. M.; McAlexander, H. R.; Kumar, A.; Saitow, M.; Wang, X.; Pritchard, B. P.; Verma, V.; Schaefer, H. F., III; Patkowski, K.; King, R. A.; Valeev, E. F.; Evangelista, F. A.; Turney, J. M.; Crawford, T. D.; Sherrill, C. D. PSI4 1.1: An Open-Source Electronic Structure Program Emphasizing Automation, Advanced Libraries, and Interoperability. *J. Chem. Theory Comput.* **2017**, *13*, 3185.

(107) Giannozzi, P.; Baroni, S.; Bonini, N.; Calandra, M.; Car, R.; Cavazzoni, C.; Ceresoli, D.; Chiarotti, G. L.; Cococcioni, M.; Dabo, I.; Dal Corso, A. D.; de Gironcoli, S.; Fabris, S.; Fratesi, G.; Gebauer, R.; Gerstmann, U.; Gougoussis, C.; Kokalj, A.; Lazzeri, M.; Martin-Samos, L.; Marzari, N.; Mauri, F.; Mazzarello, R.; Paolini, S.; Pasquarello, A.; Paulatto, L.; Sbraccia, C.; Scandolo, S.; Sclauzero, G.; Seitsonen, A. P.; Smogunov, A.; Umari, P.; Wentzcovitch, R. M. QUANTUM ESPRESSO: a modular and open-source software project for quantum simulations of materials. *J. Phys.: Condens. Matter* **2009**, *21*, 395502.

(108) Ozaki, T.; Kino, H.; Yu, J.; Han, M.; Ohfuchi, M.; Ishii, F.; Sawada, K.; Ohwaki, T.; Weng, H.; Toyoda, M.; Okuno, Y.; Perez, R.; Bell, P.; Xiao, Y.; Ito, A.; Terakura, K. *User's Manual of OpenMX Ver. 3.8*, 2016.

(109) Dey, T. K.; Shah, N. R. On the number of simplicial complexes in Rd. *Comput. Geom.* **1997**, *8*, 267.

(110) Adams, C. C.; Franzosa, R. D. *Introduction to Topology: Pure and Applied*; Pearson, 2008.

(111) Berger, M.; Pansu, P.; Berry, J.-P.; Saint-Raymond, X. Affine spaces. *Problems in Geometry*; Springer, 1984; p 11.

(112) Moon, J. W.; Moser, L. On cliques in graphs. *Isr. J. Math.* **1965**, *3*, 23−28.

(113) Balas, E.; Yu, C. S. Finding a maximum clique in an arbitrary graph. *SIAM J. Comput.* **1986**, *15*, 1054−1068.

(114) Campbell, J. E. On a Law of Combination of Operators (Second Paper) *. *Proc. London Math. Soc.* **1897**, *s1−29*, 14−32.

(115) Baker, H. F. Further Applications of Metrix Notation to Integration Problems. *Proc. London Math. Soc.* **1901**, *s1−34*, 347−360.

(116) Eichler, M. A new proof of the Baker-Campbell-Hausdorff formula. *J. Math. Soc. Jpn.* **1968**, *20*, 23−25.

(117) Trotter, M. F. On the Product of Semi-Groups of Operators. *Proc. Am. Math. Soc.* **1959**, *10*, 545.

(118) Nelson, E. Feynman Integrals and the Schrödinger Equation. *J. Math. Phys.* **1964**, *5*, 332.

(119) Otto, F. Multi-layer Potfit: An accurate potential representation for efficient high-dimensional quantum dynamics. *J. Chem. Phys.* **2014**, *140*, 014106.

(120) Wodraszka, R.; Carrington, T. Systematically expanding nondirect product bases within the pruned multi-configuration time-dependent Hartree (MCTDH) method: A comparison with multi-layer MCTDH. *J. Chem. Phys.* **2017**, *146*, 194105.

(121) Alış, Ö. F.; Rabitz, H. Efficient implementation of high dimensional model representations. *J. Math. Chem.* **2001**, *29*, 127−142.

(122) Manzhos, S.; Carrington, T., Jr. Using neural networks, optimized coordinates, and high-dimensional model representations to obtain a vinyl bromide potential surface. *J. Chem. Phys.* **2008**, *129*, 224104.

(123) Avila, G.; Carrington, T. Using a pruned basis, a non-product quadrature grid, and the exact Watson normal-coordinate kinetic energy operator to solve the vibrational Schrödinger equation for C2H4. *J. Chem. Phys.* **2011**, *135*, 064101.

(124) Avila, G.; Carrington, T. Using nonproduct quadrature grids to solve the vibrational Schrödinger equation in 12D. *J. Chem. Phys.* **2011**, *134*, 054126.

(125) Wang, X.; Carter, S.; Bowman, J. M. Pruning the Hamiltonian Matrix in MULTIMODE: Test for C2H4 and Application to CH3NO2 Using a New Ab Initio Potential Energy Surface. *J. Phys. Chem. A* **2015**, *119*, 11632−11640.

(126) Jäckle, A.; Meyer, H.-D. Product representation of potential energy surfaces. *J. Chem. Phys.* **1996**, *104*, 7974−7984.

(127) Jäckle, A.; Meyer, H.-D. Product representation of potential energy surfaces. II. *J. Chem. Phys.* **1998**, *109*, 3772−3779.

(128) Collins, M. A. Can Systematic Molecular Fragmentation Be Applied to Direct Ab Initio Molecular Dynamics? *J. Phys. Chem. A* **2016**, *120*, 9281.

(129) Schollwöck, U. The density-matrix renormalization group in the age of matrix product states. *Ann. Phys.* **2011**, *326*, 96−192 January 2011 Special Issue.

(130) White, S. R. Density matrix formulation for quantum renormalization groups. *Phys. Rev. Lett.* **1992**, *69*, 2863−2866.

(131) Vidal, G. Efficient Classical Simulation of Slightly Entangled Quantum Computations. *Phys. Rev. Lett.* **2003**, *91*, 147902.

(132) Ekert, A.; Knight, P. L. Entangled quantum systems and the Schmidt decomposition. *Am. J. Phys.* **1995**, *63*, 415−423.

(133) Mintert, F.; Viviescas, C.; Buchleitner, A. Basic Concepts of Entangled States. In *Entanglement and Decoherence: Foundations and Modern Trends*; Buchleitner, A., Viviescas, C., Tiersch, M., Eds.; Springer Berlin Heidelberg, 2009.

(134) Pathak, A. *Elements of Quantum Computation and Quantum Communication*; Taylor & Francis, 2013.

(135) Huang, Z.; Kais, S. Entanglement as measure of electron-electron correlation in quantum chemistry calculations. *Chem. Phys. Lett.* **2005**, *413*, 1−5.

(136) Wang, H.; Kais, S. Quantum Entanglement and Electron Correlation in Molecular Systems. *Isr. J. Chem.* **2007**, *47*, 59−65.

(137) Eisert, J.; Cramer, M.; Plenio, M. B. Colloquium: Area laws for the entanglement entropy. *Rev. Mod. Phys.* **2010**, *82*, 277−306.

(138) Baiardi, A.; Reiher, M. Large-scale quantum dynamics with matrix product states. *J. Chem. Theory Comput.* **2019**, *15*, 3481−3498.

(139) Delahaye, T.; Nikitin, A.; Rey, M.; Szalay, P. G.; Tyuterev, V. G. A new accurate ground-state potential energy surface of ethylene and predictions for rotational and vibrational energy levels. *J. Chem. Phys.* **2014**, *141*, 104301.

(140) Raab, A.; Worth, G. A.; Meyer, H.-D.; Cederbaum, L. Molecular dynamics of pyrazine after excitation to the S2 electronic state using a realistic 24-mode model Hamiltonian. *J. Chem. Phys.* **1999**, *110*, 936−946.

(141) Richings, G. W.; Habershon, S. Direct grid-based quantum dynamics on propagated diabatic potential energy surfaces. *Chem. Phys. Lett.* **2017**, *683*, 228−233.

(142) Polyak, I.; Richings, G. W.; Habershon, S.; Knowles, P. J. Direct quantum dynamics using variational Gaussian wavepackets and Gaussian process regression. *J. Chem. Phys.* **2019**, *150*, 041101.

(143) Nagle, J. F.; Morowitz, H. J. Molecular Mechanisms for Proton Transport in Membranes. *Proc. Natl. Acad. Sci. U.S.A.* **1978**, *75*, 298.

(144) Baciou, L.; Michel, H. Interruption of the water chain in the reaction center from Rhodobacter sphaeroides reduces the rates of the proton uptake and of the second electron transfer to QB. *Biochemistry* **1995**, *34*, 7967−7972.

(145) Guo, H.; Barnard, A. S. Proton transfer in the hydrogen-bonded chains of lepidocrocite: a computational study. *Phys. Chem. Chem. Phys.* **2011**, *13*, 17864.

(146) Domene, C.; Sansom, M. S. Potassium channel, ions, and water: simulation studies based on the high resolution X-ray structure of KcsA. *Biophys. J.* **2003**, *85*, 2787−2800.

(147) Mann, D. J.; Halls, M. D. Water Alignment and Proton Conduction inside Carbon Nanotubes. *Phys. Rev. Lett.* **2003**, *90*, 195503.

(148) Song, W.; Joshi, H.; Chowdhury, R.; Najem, J. S.; Shen, Y.-X.; Lang, C.; Henderson, C. B.; Tu, Y.-M.; Farell, M.; Pitz, M. E.; Maranas, C. D.; Cremer, P. S.; Hickey, R. J.-I.; Sarles, A. S.; Hou, J.; Aksimentiev, A.; Kumar, M. Artificial water channels enable fast and selective water permeation through water-wire networks. *Nat. Nanotechnol.* **2020**, *15*, 73−79.

(149) Hummer, G.; Rasaiah, J. C.; Noworyta, J. P. Water conduction through the hydrophobic channel of a carbon nanotube. *Nature* **2001**, *414*, 188−190.

(150) Ye, Y.-S.; Rick, J.; Hwang, B.-J. Water soluble polymers as proton exchange membranes for fuel cells. *Polymers* **2012**, *4*, 913−963.

https://doi.org/10.1021/acs.jctc.2c00484
J. Chem. Theory Comput. 2022, 18, 7243−7259

(151) Tuckerman, M. E.; Ungar, P. J.; von Rosenvinge, T.; Klein, M. L. Ab Initio Molecular Dynamics Simulations. *J. Phys. Chem.* **1996**, *100*, 12878.
(152) Tuckerman, M.; Laasonen, K.; Sprik, M.; Parrinello, M. Ab Initio Molecular Dynamics Simulation of the Solvation and Transport of H3O+ and OH- Ions in Water. *J. Phys. Chem.* **1995**, *99*, 5749.
(153) Schmitt, U. W.; Voth, G. A. The computer simulation of proton transport in water. *J. Chem. Phys.* **1999**, *111*, 9361−9381.
(154) Schmitt, U. W.; Voth, G. A. Multistate empirical valence bond model for proton transport in water. *J. Phys. Chem. B* **1998**, *102*, 5547−5551.
(155) Shin, J.-W.; Hammer, N. I.; Diken, E. G.; Johnson, M. A.; Walters, R. S.; Jaeger, T. D.; Duncan, M. A.; Christie, R. A.; Jordan, K. D. Infrared Signature of Structures Associated with the H + (H 2 O) n (n = 6 to 27) Clusters. *Science* **2004**, *304*, 1137.
(156) Headrick, J. M.; Diken, E. G.; Walters, R. S.; Hammer, N. I.; Christie, R. A.; Cui, J.; Myshakin, E. M.; Duncan, M. A.; Johnson, M. A.; Jordan, K. Spectral Signatures of Hydrated Proton Vibrations in Water Clusters. *Science* **2005**, *308*, 1765.
(157) Agmon, N. The Grotthuss Mechanism. *Chem. Phys. Lett.* **1995**, *244*, 456.

https://doi.org/10.1021/acs.jctc.2c00484
J. Chem. Theory Comput. 2022, 18, 7243−7259